Diagnostic Evaluation of Effects of Vertical Mixing on Meridional Overturning Circulation in an Idealized Ocean

Yutaka Yoshikawa*

Graduate School of Science, Kyoto University, Kyoto, Japan

Takao Kawasaki and Hiroyasu Hasumi

Atmosphere Ocean Research Institute, The University of Tokyo

published from Journal of Oceanography (https://doi.org/10.1007/s10872-021-00596-4)

* *Corresponding author address:* Graduate School of Science, Kyoto University, Kitashirakawa-Oiwake, Sakyo, Kyoto 606-8502, Japan

E-mail: yosikawa@kugi.kyoto-u.ac.jp

ABSTRACT

In this study, diagnostic equations are proposed to quantitatively evaluate meridional overturning circulation (MOC) simulated in ocean general circulation models (OGCMs). Applicability of the equations is illustrated by revisiting the MOC simulated in an idealized ocean. The simulations with surface differential heating/cooling show that, for certain horizontal distribution of vertical diffusivity, the stronger vertical mixing does not intensify the MOC while it makes the deeper water less dense. This result, which is in marked contrast to the widely accepted idea that the stronger vertical mixing promotes upwelling and intensifies the MOC by making the deeper water less dense, was investigated using the diagnostic equations. It was found that geostrophy dominates the MOC, and the geostrophic flow normal to lateral boundaries induced intense upwelling/downwelling along the boundaries. These results indicate that the primary role played by the vertical mixing on the large-scale MOC is to change hydrostatic pressure fields (geostrophic flow fields), rather than to promote upwelling. The simulation with localized cooling on the other hand showed that the ageostrophic flows significantly contribute to small-scale features of the MOC, while the geostrophic flows determine large-scale structure of the MOC. The proposed equations will thus be useful to quantitatively diagnose the MOC dynamics in realistic OGCMs.

1. Introduction

Meridional overturning circulation (MOC), one of key ingredients for long-term variations in the Earth climate, is known to be influenced by abyssal small-scale turbulent mixing (e.g., Wunsch 2002; Kuhlbrodt 2008). Numerical experiments of two-dimensional overturning circulation forced by differential surface heating and cooling (e.g., Beardsley and Festa 1972; Rossby 1998) suggest that, if the turbulent mixing was weak, a deeper ocean would be filled with colder water, and the newly formed coldest surface water would have less (negative) buoyancy to sink vigorously into the deeper ocean, hence making overturning circulation weaker in the deeper layer. Thus, stronger mixing sustains the overturning circulation by transporting (positive) buoyancy to the deeper layer and inducing buoyancy torque necessary to drive the MOC.

Intensity of the turbulent mixing can be estimated from the vertical temperature profile in the real ocean. Based on a balance between advection and diffusion of potential temperature (T) in the vertical direction

$$w\frac{\partial T}{\partial z} = \frac{\partial}{\partial z}\left(K_V\frac{\partial T}{\partial z}\right), \tag{1}$$

and a gross estimate of an upwelling velocity ($w \simeq 10^{-6}$ m s^{-1}), Munk (1966) pointed out that the vertical eddy diffusivity K_V of $\mathscr{O}$ (10^{-4} m^2 s^{-1}), which is much larger than the molecular diffusivity of $\mathscr{O}$ (10^{-7} m^2 s^{-1}), is necessary to explain the observed vertical profile of potential temperature gradient ($\partial T/\partial z$). Thus, the turbulent mixing sustains the thermocline structure and the MOC in the real ocean. This is also supported by numerical simulations of the three-dimensional ocean general circulation model (OGCM) where the larger K_V corresponds to the more intense MOC (e.g., Bryan 1987).

The large impact of the vertical mixing on the MOC shed light on small-scale turbulent mixing in the abyssal ocean. Extensive efforts have been made to reveal magnitude and distribution of

K_V in the real abyssal ocean through direct and indirect measurements of the dissipation rates of turbulent kinetic energy (e.g., Waterhouse et al. 2014). The estimated K_Vs in the abyssal ocean are found to range from 10^{-5} m^2 s^{-1} in the thermocline (e.g., Ledwell and Law 1993; Ledwell et al. 1998) to greater than 10^{-3} m^2 s^{-1} in the deep ocean above regions of rough topography (e.g., Polzin et al. 1997; Ledwell et al. 2000). Large K_Vs were also estimated at around 30° latitude (e.g., Hibiya et al. 2007). These patterns can be interpreted in terms of the geography of internal wave generation, propagation, interactions and dissipation (e.g. MacKinnon et al. 2017). Noteworthy is that the estimated K_Vs by these field measurements are overall smaller than $\mathcal{O}$ (10^{-4} m^2 s^{-1}) expected from the temperature gradient mentioned above (e.g., Munk and Wunsch 1998). Wind-induced mechanical upwellings in the Southern Ocean (e.g., Webb and Suginohara 2001) seem partly responsible for this gap. Another ingredient is inhomogeneity in K_V, as numerical studies (e.g., Tsujino et al. 2000; Jayne 2009) have shown that such spatial inhomogeneity in K_V has noticeable impact on the MOC.

Large impacts of the vertical mixing on the MOC described above are sometimes interpreted as "vertical mixing makes deeper water less dense, promoting upwelling" (e.g., Visbeck 2007) or vertical mixing "pulls" deeper water (e.g., Kuhlbrodt 2008). This interpretation is helpful to highlight the impact of one important ingredient for the MOC – the small-scale vertical mixing. However, another essential ingredient for large-scale ocean circulation, geostrophy, needs to be considered, as the geostrophic flows are dominant in the three-dimensional global overturning circulations (e.g., Bryan 1987; Zhang et al. 1992; Marotzke 1997). Significant roles of the geostrophic flows as well as the vertical mixing in the MOC were demonstrated in numerical experiments of Marotzke (1997) and Scott and Marotzke (2002) where the vertical mixing along side boundaries was shown to have large impacts on east - west density differences and hence meridional geostrophic flows through the thermal wind balance. Convective mixing along boundaries, which changes along-boundary buoyancy gradient and hence induces cross-boundary geostrophic flows through the thermal wind relation, is also suggested to be related to the MOC (e.g., Spall and Pickart 2001; Katsman et al. 2018). However, relative contributions from the geostrophic process and ageostrophic process (that could be particularly large near the boundaries) in the MOC remain unquantified. This leaves our understanding of the MOC dynamics and a role played by the vertical mixing and the geostrophic flow in it vague.

The aim of this study is to quantitatively evaluate the geostrophic and ageostrophic processes in the MOC using diagnostic equations derived in the present study. To this aim, we revisited the three-dimensional thermohaline circulations in an idealized rectangular ocean that have been investigated in many previous studies (e.g., Bryan 1987; Zhang et al. 1992; Marotzke 1997; Park and Bryan 2000; Scott and Marotzke 2002). In section 2, numerical model configuration is described. The circulations driven by surface differential heating/cooling are presented in section 3 where locally increased vertical diffusivity is found to slightly weaken MOC while making deeper water less dense. This result, which is in marked contrast to the widely accepted idea of "pull by the mixing", was investigated quantitatively using a proposed diagnostic vorticity balance equation. The vorticity equation highlights effects of the vertical mixing on large-scale hydrostatic pressure field (geostrophic flows), rather than on the vertical velocity that could be directly impacted through the advection - diffusion equation of temperature. The diagnostic equation for simulated vertical velocity was also derived to decompose the velocity into three parts, the component due to the planetary vorticity change, the component induced by ageostrophic advection and viscosity, and the component caused by the geostrophic flow normal to the boundary, to show that the last component dominantly shapes the large-scale structure of the MOC. Heat balances in the vertical direction are also examined in this section. In section 4, the circulation driven by localized cooling is shown to illustrate that the ageostrophic flows could be significant for the small-scale features of the MOC. Finally, concluding remarks and discussions are given in section 5.

2. Model Configuration

A simple rectangular ocean of dimension $L(=6400$ km$)$ in both the zonal and the meridional directions and $D=(4000$ m$)$ in the vertical direction on a β-plane was considered. The ocean surface was assumed to be rigid. With the hydrostatic approximation, the governing equations for a Boussinesq ocean are given by

$$\frac{\partial u}{\partial t}+\mathscr{A}(u)-fv=-\frac{\partial}{\partial x}\frac{p}{\rho_0}+\mathscr{V}(u) \tag{2}$$

$$\frac{\partial v}{\partial t}+\mathscr{A}(v)+fu=-\frac{\partial}{\partial y}\frac{p}{\rho_0}+\mathscr{V}(v) \tag{3}$$

$$0=-\frac{\partial}{\partial z}\frac{p}{\rho_0}+\alpha gT \tag{4}$$

$$\frac{\partial u}{\partial x}+\frac{\partial v}{\partial y}+\frac{\partial w}{\partial z}=0 \tag{5}$$

$$\frac{\partial T}{\partial t}+\mathscr{A}(T)=\mathscr{D}(T)+F_T \tag{6}$$

$$\mathscr{A}(\bullet)=\frac{\partial u\bullet}{\partial x}+\frac{\partial v\bullet}{\partial y}+\frac{\partial w\bullet}{\partial z} \tag{7}$$

$$\mathscr{V}(\bullet)=A_H\left(\frac{\partial^2\bullet}{\partial x^2}+\frac{\partial^2\bullet}{\partial y^2}\right)+A_V\frac{\partial^2\bullet}{\partial z^2} \tag{8}$$

$$\mathscr{D}(\bullet)=K_H\left(\frac{\partial^2\bullet}{\partial x^2}+\frac{\partial^2\bullet}{\partial y^2}\right)+K_V\frac{\partial^2\bullet}{\partial z^2} \tag{9}$$

where x (eastward), y (northward) and z (upward) are Cartesian coordinates with the origin $(x,y,z)=(0,0,0)$ at the surface southwest corner, t is time, u, v and w are velocity in the x, y and z directions, respectively, p is pressure, T is potential temperature, f $(=\beta y)$ is the Coriolis parameter ($\beta=2.0\times10^{-11}$ m^{-1} s^{-1}) , ρ_0 ($=1000$ kg m^{-3}) is a reference water density, g ($=10$ m s^{-2}) is the gravitational acceleration, and α ($=2.0\times10^{-4}$ K^{-1}) is a thermal expansion coefficient of water. Here the equation of state was linearized ($\rho/\rho_0=1-\alpha T$) while neglecting salinity effects on density (ρ) for simplicity. Horizontal and vertical eddy viscosities (A_H and A_V) were set as 4×10^4 and 1×10^{-2} m^2 s^{-1}, respectively. Horizontal eddy diffusivity (K_H) was set as 4×10^2 m^2 s^{-1}, and vertical eddy diffusivity (K_V) was set as 1×10^{-4} m^2 s^{-1} unless otherwise noted. Static stability was removed by convective adjustment, by increasing the vertical eddy diffusivity to 1×10^{-2} m^2 s^{-1} wherever $\partial T/\partial z < 0$. The last term in Eq. (6) represents thermal forcing whose specific form is described in the following sections. The model ocean is forced only by this thermal forcing. (No wind forcing was imposed.) At the boundary, no normal flow, free-slip, and insulating conditions were applied.

The governing equations and boundary conditions were approximated with a second-order finite difference scheme with the Arakawa-C grid. Grid spacing was 100 km in the horizontal direction and 100 m in the vertical direction. Time integration was performed with the second-order Runge-Kutta scheme with time step of 5400 s. Other model configurations (e.g., specific form of F_T and initial condition) are described in the following sections.

3. Experiments With Surface Differential Heating/Cooling

In this section, the MOC driven by surface differential heating/cooling was investigated. For this purpose, the thermal forcing was set as

$$F_T = \gamma(SST - T)\delta_z, \tag{10}$$

$$SST = \Delta T\,(1 - y/L)\,, \tag{11}$$

where $\delta_z = 1$ in the top surface grid box and $\delta_z = 0$ in the other subsurface grid boxes. The restoring time γ^{-1} was set as 10 days. Initially, the model ocean was at rest and the temperature was uniformly set at $0\,^\circ$ C. The MOC, quantitative definition of which will be given later, reached an almost steady state by $t = 4000$ years. To illustrate how the vertical mixing alters the MOC, we increased the vertical eddy diffusivity locally at and after $t = 4000$ years, and continued numerical integration until $t = 7000$ years; by then the MOCs influenced by the increased K_V reached another steady state. For comparison, we also continued the original (K_V unchanged) experiment until $t = 7000$ years. Results at $t = 7000$ years are presented below. Note that these simulations are meant to illustrate the potential impacts of the vertical mixing and the geostrophic flows on the MOC rather than to simulate realistic MOC influenced by complicated inhomogeneity in K_V.

a. Temperature and Velocity Fields

First, to overview the simulated circulation driven by the differential surface heating/cooling, temperature and velocity fields are briefly described. Note that they are essentially the same with those of the previous studies. Figure 1 shows horizontal fields of the temperature and flows in the experiment with constant K_V (referred to as a base experiment or B experiment). Due to the surface restoring forcing, zonal structure of the temperature is evident near the surface ($z = -150$ m) (Figure 1a). Slight deviations from the zonal structure reflect advection by the flow. The surface flow was eastward at $y \geq 3000$ km, which was in thermal wind balance with the meridional temperature (buoyancy) gradient. The eastward surface flow induced strong upwelling and downwelling at the western and eastern boundary, respectively (Figure 1c). The upwelling contributed to the surface water cooling near the western boundary. At $y \leq 1500$ km, the surface flow was westward, partly compensating the eastward flow to the north. These zonal currents and an intense northward western boundary current form a surface anti-cyclonic circulation in the surface layer. At $z = -1150$ m, (Figures 1b and d), warm temperature anomaly was apparent near the downwelling region along the eastern boundary. This temperature anomaly or lowered thermocline was propagated southwestward (Figure 1b). The circulation at greater depths was cyclonic, with an intense southward western boundary current.

Figure 2 shows vertical sections of the temperature. A meridional-vertical distribution of zonally averaged temperature (Figure 2a) shows thermocline formed above 500 m depth, with the temperature being less than 2 $^\circ$ C below 800 m. A zonal vertical section of the temperature averaged over 4600 km $\leq y \leq$ 5000 km (Figure 2b) shows tilting (eastward deepening) of the thermocline.

The MOC was quantified by volume transport stream function Φ defined as

$$\int_0^L v dx = -\frac{\partial \Phi}{\partial z}. \tag{12}$$

The function, calculated by vertically integrating the above equation with $\Phi = 0$ at the bottom ($z = -D$), is shown in Figure 2c. The northward and southward transports are evident above and below the thermocline, respectively, which are supported by the eastward deepening thermocline (Figure 2b) through the thermal wind relation. The largest Φ (10.03 Sv) is found at around $y = 5000$ km, to the north (south) of which the thermocline is weakly (strongly) stratified (Figure 2a). All these features are consistent with the previous numerical experiments (e.g., Bryan 1987; Marotzke 1997; Spall and Pickart 2001; Zhang et al. 1992; Scott and Marotzke 2002).

To illustrate the impacts of the vertical mixing and geostrophy on Φ, we performed two experiments in which K_v was increased to be 10^{-2} m^2 s^{-1} (100 times larger than the original K_v) at $4600 \leq y \leq 5000$ km along the western ($x \leq 200$ km) and the eastern ($x \geq 6200$ km) boundaries, respectively. Note that area of the K_V intensified region (hereafter referred to as the intensified mixing region) and hence the area-averaged K_V were the same in these two experiments. Results of the experiment with increased K_V at the western boundary (hereafter referred to as W experiment) are shown in Figures 3 and 4. Horizontal temperature and flow fields in the W experiment (Figures 3a and b) were overall similar to those of the B experiment (Figure 1). Slight deviations from the B experiment, however, reveal effects of the increased K_V. The increased K_v decreased (increased) temperature at shallower (greater) depths in the intensified mixing region. In the W experiment, the temperature decrease occurred at $z \geq -100$ m, and positive temperature anomaly from the B experiment was found at $z \leq -100$ m in the intensified mixing region (Figure 4b). The positive temperature anomaly corresponds to lowered thermocline, and this lowered thermocline propagated southward as the Kelvin wave along the western boundary (Figures 3a and b). This deepening of the thermocline along the western boundary resulted in reducing zonal tilt of the thermocline and consequently the northward (southward) western boundary current in the upper (lower) thermocline (Figures 3c and d).

The temperature anomaly was propagated cyclonically along the boundaries, and the thermocline in southern region was overall deepened (Figures 3a and b). This resulted in increasing eastward (westward) current in the upper (lower) thermocline (Figures 3c and d) through the thermal wind balance. As a consequence, downwelling velocity at around $y = 5500$ km at the eastern boundary was intensified, and the thermocline there was deepened (Figure 3b). The MOC (Figure 4c) was influenced by these processes. Due to the intensified downwelling at around $y = 5500$ km, Φ to the north of $y = 5000$ km was slightly increased. However, Φ to the south of $y = 5000$ km was greatly decreased, with the reduced northward western boundary current being responsible for this decrease. The decrease to the south of $y = 4600$ km was much larger than the increase to the north of $y = 5000$ km, and hence the largest Φ was 10.00 Sv, slightly smaller than that in the B experiment. Thus, the increased K_V did not intensify the MOC, despite the deeper water warming (Figure 4a). This is in marked contrast with the idea that vertical mixing promotes upwelling by making deeper water less dense.

Results of the experiment with increased K_V at the eastern boundary (hereafter referred to as E experiment) are shown in Figures 5 and 6. Horizontal temperature and flow fields (Figure 5) were similar to those of the B and W experiments, but deviations from the B experiment were different from W experiment. The temperature in the intensified mixing region decreased above (increases below) $z = -800$ m (Figure 6b), and these deviations propagated northward along the eastern boundary as the Kelvin waves and southwestward as the Rossby waves. Eastward deepening of the thermocline became steeper, intensifying the northward (southward) geostrophic flow in the upper (lower) thermocline. This resulted in increased MOC (Figure 6c).

All these results are consistent with the results of Scott and Marotzke (2002); intensified vertical mixing along the eastern boundary causes larger MOC than the intensified mixing along the western boundary. Dynamical processes described above were also given by Scott and Marotzke (2002) in more details. The point to emphasize in this study is the fact that locally intensified vertical mixing (increased K_V), which makes deeper water less dense, does not always intensify global-scale MOC (promote upwelling). To quantitatively examine the mixing and the MOC on dynamical framework, a dynamical balance equation for the MOC is derived and diagnosed in the next subsection.

b. Vorticity Balance

Lee and Marotzke (1998) decomposed the MOC (Φ) into three components: a geostrophic shear component, an Ekman component, and a barotropic current component in a heuristic way, and discussed structure and variation of simulated MOC in the Indian ocean. Later studies (e.g., Hirschi and Marotzke 2007) used this decomposition to discuss the global MOC. Although this approach is successful at providing framework of the MOC dynamics, the dynamics remains less quantified because the decomposition was derived heuristically. In this study, in order to make more rigorous discussion on the MOC dynamics, a diagnostic equation for vorticity balance of the MOC is derived from the governing equations. In deriving the equation, arbitrary bottom topography is assumed, which will allow future application of the equation to more realistic simulations. We use the equation to understand how the increased K_v changed MOC described in the previous subsection.

Cross differentiation of Eqs. (2) and (4) with respect to x and z and Eqs. (3) and (4) with respect to y and z respectively yields

$$\frac{\partial}{\partial t}\frac{\partial u}{\partial z} - f\frac{\partial v}{\partial z} = -\alpha g\frac{\partial T}{\partial x} - \frac{\partial \mathscr{A}(u) - \mathscr{V}(u)}{\partial z} \tag{13}$$

$$\frac{\partial}{\partial t}\frac{\partial v}{\partial z} + f\frac{\partial u}{\partial z} = -\alpha g\frac{\partial T}{\partial y} - \frac{\partial \mathscr{A}(v) - \mathscr{V}(v)}{\partial z} \tag{14}$$

Further manipulation ($\partial(14)/\partial t - f \times (13)$ and $\partial(13)/\partial t + f \times (14)$) results in

$$\left(\frac{\partial^2}{\partial t^2} + f^2\right)\frac{\partial v}{\partial z} = \frac{\partial}{\partial t}\left[-\alpha g\frac{\partial T}{\partial y} - \frac{\partial \mathscr{A}(v) - \mathscr{V}(v)}{\partial z}\right] - f\left[-\alpha g\frac{\partial T}{\partial x} - \frac{\partial \mathscr{A}(u) - \mathscr{V}(u)}{\partial z}\right] \tag{15}$$

$$\left(\frac{\partial^2}{\partial t^2} + f^2\right)\frac{\partial u}{\partial z} = \frac{\partial}{\partial t}\left[-\alpha g\frac{\partial T}{\partial x} - \frac{\partial \mathscr{A}(u) - \mathscr{V}(u)}{\partial z}\right] + f\left[-\alpha g\frac{\partial T}{\partial y} - \frac{\partial \mathscr{A}(v) - \mathscr{V}(v)}{\partial z}\right] \tag{16}$$

Zonal integration of Eq. (15) from the western boundary $x = X_W$ ($= 0$ in the present study) to the eastern boundary $x = X_E$ ($= L$) yields [1]

$$\begin{aligned}\left(\frac{\partial^2}{\partial t^2} + f^2\right)\frac{\partial^2 \Phi}{\partial z^2} = \frac{\partial}{\partial t}&\left[\alpha g\int_{X_W}^{X_E}\frac{\partial T}{\partial y}dx + \int_{X_W}^{X_E}\frac{\partial \mathscr{A}(v) - \mathscr{V}(v)}{\partial z}dx\right] \\ &- f\left[\alpha g(T_E - T_W) + \int_{X_W}^{X_E}\frac{\partial \mathscr{A}(u) - \mathscr{V}(u)}{\partial z}dx\right] \\ &- \left(\frac{\partial^2}{\partial t^2} + f^2\right)\left(\frac{\partial X_E}{\partial z}v_E - \frac{\partial X_W}{\partial z}v_W\right)\end{aligned} \tag{17}$$

where

$$\frac{\partial \Phi}{\partial z} = -\int_{X_W}^{X_E} v\,dx \tag{18}$$

is the meridional volume transport function (which reduces to Eq. (12) in the present model configuration), T_E (T_W) and v_E (v_W) are temperature and meridional velocity at the eastern (western) boundary $x = X_E$ (X_W), respectively. It should be noted that K_V (or $\mathscr{D}(T)$ in Eq. 6) does not appear in the above equation. It affects $\partial^2\Phi/\partial z^2$ (and hence Φ) through $\partial T/\partial y$ and/or $T_E - T_W$. It should

[1]Meridional integration of Eq. (16) provides diagnostic equation of zonal overturning circulation.

be also noted that Eq. (17) is nonlinear in terms of Φ; it is implicitly included in the right hand side of Eq. (17). Therefore, Eq. (17) was used to diagnose vorticity balance rather than to solve Φ itself.

To illustrate vorticity dynamics described in Eq. (17), let us first consider the MOC in the non-rotating ($f=0$) flat ocean, referred to as horizontal convection (e.g., Hughes and Griffiths 2008). In this case, Eq. (17) reduces to

$$\frac{\partial}{\partial t}\frac{\partial^2\Phi}{\partial z^2} = \alpha g \int_{X_W}^{X_E} \frac{\partial T}{\partial y} dx + \int_{X_W}^{X_E} \frac{\partial \mathscr{A}(v)}{\partial z} dx - \mathscr{V}\left(\frac{\partial^2\Phi}{\partial z^2}\right), \tag{19}$$

where $\Phi=0$ at $t=0$ is assumed. This equation shows that Φ is forced by zonally integrated meridional torque associated with the temperature gradient ($\alpha g \partial T/\partial y$), damped by viscous diffusion ($\mathscr{V}(\partial^2\Phi/\partial z^2)$), and modified by zonally-integrated vertically-differentiated advection of the meridional velocity ($\partial\mathscr{A}(v)/\partial z$). The advection term tends to shift the center of the circulation toward the sinking region (surface cooling region) and upward (e.g., Rossby 1998). The meridional temperature gradient, the driver of the MOC, is forced by the surface differential heating / cooling. The temperature distribution below the surface is determined by advection and diffusion of the temperature. The advection transports colder (warmer) water to greater (shallower) depths, while the diffusion or the vertical mixing K_V makes the surface temperature gradient to penetrate to greater depths. Without K_V, the advection makes deeper ocean filled with the cold water, and the temperature gradient (the meridional torque) and the MOC are weak in the deeper layer. Thus, K_V acts to penetrate the torque and strengthen the MOC at greater depths. This explains the overall mechanisms of the two-dimensional MOC (or horizontal convection), that is, push (surface cooling and advection) or pull (surface heating and diffusion) determine the intensity of the MOC.

In the rotating case, on the other hand, the Coriolis acceleration alters dynamical balances. In a steady state, Eq. (17) reduces to

$$f\frac{\partial^2\Phi}{\partial z^2} = -\alpha g(T_E - T_W) - \int_{X_W}^{X_E} \frac{\partial \mathscr{A}(u) - \mathscr{V}(u)}{\partial z} dx - f\left(\frac{\partial X_E}{\partial z} v_E - \frac{\partial X_W}{\partial z} v_W\right) \tag{20}$$

A balance between the left-hand side term and the first term in the right hand side is the thermal wind balance. Deviation from the balance is caused by zonally-integrated vertically-differentiated advection and viscous diffusion of the zonal velocity (the second term on the right hand side), and terms associated with variable bottom topography (the last term on the right hand side). The bottom topography term corresponds to the barotropic component discussed in Lee and Marotzke (1998), which is nonzero if the bottom ocean is not flat. The Ekman component (Lee and Marotzke 1998) is forced by a zonal wind stress, which is represented by the $\mathscr{V}(u)$ term. The above equation is more rigorous than the equation used in Lee and Marotzke (1998) in that it is derived from the governing equations. The equation (20) enables us to make quantitative analysis of the MOC dynamics.

We evaluated each term in Eq. (17) in the B experiment with $X_W = 0$ and $X_E = L$ (Figure 7). In the figure, the second time derivative on the left-hand side was ignored, due to longer time scales of the MOC than the inertial period (f^{-1}). This approximation corresponds to the planetary geostrophic approximation that was validated for the large-scale MOC by Zhang et al. (1992). It is clear from this figure that the thermal wind balance dominated the vorticity balance; geostrophy dominates MOC (Φ). This is illustrated by geostrophic (Φ_g) and ageostrophic (Φ_a) volume transport functions shown in Figure 8, where the geostrophic velocity (u_g, v_g) and the ageostrophic velocity were defined as

$$u_g = -\frac{1}{\rho_0 f}\frac{\partial p}{\partial y}, v_g = \frac{1}{\rho_0 f}\frac{\partial p}{\partial x}, \tag{21}$$

$$u_a = u - u_g, \qquad v_a = v - v_g, \tag{22}$$

and Φ_g and Φ_a were calculated by vertically integrating Eq. (12) with v_g and v_a instead of v, respectively. The volume transport stream function Φ was dominated by the geostrophic component (Φ_g, calculated from v_g) except near the southern boundary (equator) where small f amplified numerical differential errors. Correspondence between Φ and Φ_g simulated in a similar idealized ocean was also demonstrated by Zhang et al. (1992) and Hirschi and Marotzke (2007). In both the W and E experiments, vorticity balance was dominated by the thermal wind balance (Figure 9). Thus in the present experiments, intensified vertical mixing does not alter dominance of the geostrophy.

These results confirm significance of the zonal tilts of the thermocline depths as the previous studies demonstrated (e.g., Zhang et al. 1992; Marotzke 1997; Park and Bryan 2000; Scott and Marotzke 2002). The (geostrophic) MOC was supported by the eastward deepening thermocline (or isopycnal surfaces), and intensity of the MOC was affected by processes that influence this thermocline tilt. In W experiment, the increased K_V (intensified mixing) deepened the thermocline at the western boundary, reducing the thermocline tilt and MOC. On the other hand, in the E experiment, the increased K_V deepened the thermocline at the eastern boundary, intensifying the thermocline tilt and MOC.

Note that horizontally uniform intensification of the vertical mixing makes the thermocline deep with less change in the thermocline tilt, resulting in deep northward geostrophic flows and intensified MOC as in the nonrotating case (e.g., Zhang et al. 1992; Park and Bryan 2000). If the intensification is horizontally nonuniform, however, the MOC, which depends greatly on the thermocline depth difference between the eastern and western boundaries, can be either intensified or weakened (e.g., Marotzke 1997; Scott and Marotzke 2002).

c. Vertical Velocity

The MOC is accompanied by upwelling/downwelling, while the geostrophic flows, the greatest component of the present MOC, are nondivergent to the first order (as the quasi-geostrophic theory shows) due to planetary vorticity constraints in the ocean interior (e.g., Spall 2000; Spall and Pickart 2001; Katsman et al. 2018). To evaluate "ageostrophic" upwelling/downwelling velocities involved in the MOC in our simulation in more quantitative manner, a diagnostic equation for the vertical velocity was derived in this study. Horizontal divergence of Eqs. (16) and (15) yields, together with (5),

$$\left(\frac{\partial^2}{\partial t^2}+f^2\right)\frac{\partial^2 w}{\partial z^2}=\frac{\partial}{\partial t}\left\{\alpha g\left(\frac{\partial^2}{\partial x^2}+\frac{\partial^2}{\partial y^2}\right)T+\frac{\partial}{\partial z}\left[\frac{\partial \mathscr{A}(u)-\mathscr{V}(u)}{\partial x}+\frac{\partial \mathscr{A}(v)-\mathscr{V}(v)}{\partial y}\right]\right\}$$
$$+f\frac{\partial}{\partial z}\left[\frac{\partial \mathscr{A}(v)-\mathscr{V}(v)}{\partial x}-\frac{\partial \mathscr{A}(u)-\mathscr{V}(u)}{\partial y}\right]+\frac{\partial f}{\partial y}\left[2f\frac{\partial v}{\partial z}-\alpha g\frac{\partial T}{\partial x}-\frac{\partial \mathscr{A}(u)-\mathscr{V}(u)}{\partial z}\right]. \quad (23)$$

Assuming $\mathscr{A}=\mathscr{V}=\partial f/\partial y=0$, this equation together with linearized buoyancy tendency equation $\alpha g\partial T/\partial t+N^2 w=0$ provides the dispersion relation of hydrostatic inertial-internal gravity waves. In a steady state, on the other hand, the above equation reduces to

$$\begin{aligned} w &= -\frac{1}{f}\int_z^0\left(\frac{\partial \mathscr{A}(v)-\mathscr{V}(v)}{\partial x}-\frac{\partial \mathscr{A}(u)-\mathscr{V}(u)}{\partial y}\right)dz-\frac{1}{f}\frac{\partial f}{\partial y}\int_z^0 v dz \\ &= \int_z^0\left(\frac{\partial u_a}{\partial x}+\frac{\partial v_a}{\partial y}\right)dz-\frac{1}{f}\frac{\partial f}{\partial y}\int_z^0 v_g dz. \end{aligned} \quad (24)$$

(In the above, the rigid-lid boundary condition ($w=0$ at $z=0$) was used.) Note that the above equations are applicable only if $f\neq 0$. (In nonrotating ($f=0$) case, not w but $\partial^2 w/\partial t^2$ or $\partial w/\partial t$ should be diagnosed from Eq. (23).) Equation (24) can also be derived directly from the steady state version of Eqs. (2), (3) and (5). The first term on the right hand side of Eq. (24) represents divergence of ageostrophic velocity $(u_a, v_a)=(-\mathscr{A}(v)+\mathscr{V}(v), \mathscr{A}(u)-\mathscr{V}(u))/f$, while the second term represents planetary vorticity change that induces stretching/shrinking of water column ($\beta v_g = f\partial w/\partial z$). (Hereafter, the last term is referred to as the Sverdrup term.) Care should be taken at lateral boundaries at which velocity normal to the boundary vanishes while the pressure gradient along the boundary (hence the geostrophic flow normal to the boundary) does not. For example, at the western or eastern boundary ($x = 0$ or L), $u = 0$ but $\partial p/\partial y = -\rho_0 f u_g$ that is generally nonzero. In the present study, $u_g \neq 0$ and $u_a = -u_g$ at the boundaries. Here we refer to this boundary ageostrophic flow that compensates the geostrophic flow normal to the boundary as a boundary ageostrophic flow. (The other ageostrophic flow is referred to as an interior ageostrophic flow.) The boundary ageostrophic flow is nonzero only on the boundary, while the interior ageostrophic flow is zero there (but nonzero in the interior). Horizontal divergence of the boundary ageostrophic flow (that is nonzero only within the one grid box adjacent to the boundaries) could be large and induce intense vertical velocity along the boundary. The vertical velocity due to the boundary ageostrophic flow was referred to as the mass-balance flow in Scott and Marotzke (2002). The pressure gradient along the boundary was induced by the surface differential cooling. Importance of the surface differential cooling along boundaries on the MOC were shown by Spall (2000) and Spall and Pickart (2001).

Figure 10 shows the diagnosed vertical velocity (the left-hand side term of Eq. (24)) as well as its three components, the interior and boundary ageostrophic components (the first term of the right hand side) and the Sverdrup component (the second term). The diagnosed vertical velocity agrees well with the simulated vertical velocity (Figure 1c), except at lower latitudes where numerical differential errors were amplified due to small f. Intense upwelling and downwelling were found along the western and eastern boundaries, respectively, which correspond to the boundary ageostrophic component. Thus, geostrophic flows (or pressure gradients along the boundary) induced intense vertical velocity along the boundary. Relatively intense vertical upwelling and downwelling were also found slightly away from the boundaries, which were driven by the viscous diffusion of (mostly geostrophic) horizontal flows $\mathscr{V}(u) \simeq \mathscr{V}(u_g)$ and $\mathscr{V}(v) \simeq \mathscr{V}(v_g)$ (not shown) in the present simulation. Away from the boundary, the interior ageostrophic component was small and the Sverdrup component shaped the horizontal distribution of the vertical velocity which was negative (downwelling) in the northern region (where the flow above the thermocline base was northward) and positive (upwelling) in the southern region (where the flow was southward). These results, being consistent with the previous studies (e.g., Spall and Pickart 2001), show that Eq. (24) enables quantitative evaluations of the geostrophic and ageostrophic processes that derives the vertical velocity.

Figure 11 shows meridional distribution of the vertical velocity components (interior ageostrophic, boundary ageostrophic, and Sverdrup components) averaged over entire zonal - vertical (x - z) section. In the B experiment, the largest contribution was the boundary ageostrophic component that was positive (upwelling) in $y \leq 5500$ km and negative (downwelling) in $y \geq 5500$ km, in agreement with the volume transport function (Φ) distribution (Figure 8). The interior ageostrophic component was large only in $y \geq 5500$ km (and $y \leq 700$ km where errors in the geostrophic calculation were large) where its sign was opposite to that of the boundary ageostrophic component. The Sverdrup component was negative everywhere (downwelling) which reflected the northward flow (convergent geostrophic flow) in the upper layer and southward flow (divergent geostrophic flow) in the lower layer. These profiles of the vertical velocity components were similar in the W and E experiments (Figure 11b and c), although the interior ageostrophic upwelling was slightly intensified in the intensified mixing region. This is due to the intensified horizontal viscous diffusion of geostrophic flows around the intensified mixing region, where the geostrophic flows were distorted because of hydrostatic pressure anomaly caused by the vertical mixing. In this way, the vertical mixing can locally intensify the upwelling through the interior ageostrophic component ($\mathscr{A} - \mathscr{V}$) (e.g., Kawasaki and Hasumi 2010). Note that this locally intensified upwelling due to the interior ageostrophic component can contribute significantly the MOC with horizontal scales smaller than the deformation radius, as will be shown in the next section. In the present experiment, the contribution of this locally intensified upwelling to the global-scale MOC was much weaker than that of the upwelling by the boundary ageostrophic component.

d. Heat Balance

To see the impact of intensified vertical mixing on the vertical heat balance (Eq. 1) that directly connects K_V and w, we examined the heat balance (Eq. 6) in the present experiments. Here, the surface restoring forcing was included in the vertical diffusion term. At first, in order to see typical heat balances in interior regions of the B experiment, the profiles in the southern and northern central regions are shown in Figures 12a and b, respectively. In the southern central region (3000 km $\leq x \leq$ 3400 km and 1400 km $\leq y \leq$ 1800 km), where the weak Sverdrup upwelling occurred (Figure 10), a major heat balance was between cooling due to vertical advection (cold water upwelling, represented by blue dashed line) and warming due to vertical diffusion (red dashed line), as described by Munk (1966), though horizontal advection and diffusion (blue and red dotted lines, respectively) also contributed to the cooling in the upper 500 m. In the northern central region (3000 km $\leq x \leq$ 3400 km and 4600 km $\leq y \leq$ 5000 km) where the weak Sverdrup downwelling occurred, on the other hand, the primary balance was between cooling due to the horizontal diffusion and warming due to the horizontal advection. The vertical advection also contributed to warming slightly, while the vertical diffusion cooled and warmed the upper ($z \geq -500$ m) and lower ($z \leq -500$ m) thermocline, respectively. Similar balances in the interior regions were also found in both the W and E experiments (not shown). Note that in the real ocean, the surface wind stress, which induces downwelling and upwelling in the subtropical and subpolar regions through Ekman pumping and suction, respectively, may change direction of the interior vertical velocity and hence the above interior heat balance.

The heat balance in the boundary regions of the B experiment is shown in Figures 12c and d. In the western boundary region ($x \leq 200$ km and 4600 km $\leq y \leq$ 5000 km, where the mixing was intensified in the W experiment), intense upwelling due to the boundary compensating flow caused intense cooling, which was balanced by the warming due to the horizontal diffusion. In the eastern boundary region ($x \geq 6200$ km and 4600 km $\leq y \leq$ 5000 km, where the mixing was intensified in the E experiment) where the downwelling due to the geostrophic flow dominated, on the other hand, the balance was established by warming due to the horizontal advection and cooling due to the vertical diffusion.

The heat balance in the W and E experiments was almost the same as that in the B experiment, except in the intensified mixing region. In the intensified mixing region of the W experiment (Figure 12e), the intensified vertical diffusion transported surface heat downward (deeper layer warming), but the heating was limited above 2000 m depth. The intensified upwelling (Figure 3c) on the other hand cooled the water except very near the surface. Horizontally divergent flow also contributed to the cooling in the upper layer ($z \geq$ -1000 m) and warming in the lower layer ($z \leq$ -1000 m). The lower layer warming due to the horizontally divergent flow was balanced by the upwelling induced cooling. In the intensified mixing region of the E experiment, on the other hand, the heat balance was complicated. Combined effects of the horizontal and vertical advection warmed (cooled) the upper (lower) thermocline above (below) $z =$ -500 m, which was balanced with the combined effects of diffusion. Near the surface, the geostrophic flows normal to the boundary transported the heat into this region, which was transported downward by the intensified downwelling and the vertical diffusion.

4. Experiment with Localized Cooling

In this section, the Stommel-Arons type thermohaline circulation (e.g., Stommel and Arons 1960) was investigated. For this purpose, the thermal forcing F_T in Eq. (6) was set as

$$F_T = \gamma(SST - T)\delta(z) + \begin{cases} \gamma\left(1+\frac{z}{D}\right)(DWT - T) & 400\text{ km } < x < 800\text{ km and } 5600\text{ km } < y < 6000\text{ km} \\ 0 & \text{otherwise} \end{cases} \tag{25}$$

where DWT (deep water temperature) $= 0°$C and $SST = 10°$C. This forcing is meant to represent deeper water formation in a localized area near the northwest corner of the ocean. Initially the model ocean was at rest and temperature was set as 10 deg. Other model configuration was the same as that in the B experiment. The integration was performed for 4000 years by which the MOC became steady. This experiment was referred to as SA experiment.

The circulation was spun up as described by Kawase (1987) (not shown), and the Stommel-Arons type thermohaline circulation established as shown by the velocity field at 3050 m depth (Figure 13) where an intense southward western boundary current (roughly at $x \leq 500$ km) and weak northward geostrophic flows in an interior region (roughly at $x \geq 1000$ km) are evident.

The MOC (Figure 14a) shows localized intense downwelling at the forcing latitude (5600 km $< y <$ 6000 km) and broad weak upwelling at other latitudes. The geostrophic and ageostrophic component of the MOC (Figure 14b and c, respectively) shows that the localized downwelling is ageostrophic while large-scale MOC is geostrophic. Zonally averaged vertical velocity (Figure 15) shows that the interior ageostrophic component dominates the localized downwelling/upwelling at around the forcing latitude, while the boundary ageostrophic component (induced by geostrophic flow normal to the boundary) forms the large-scale upwelling. Note that the zonally averaged Sverdrup component was downward at all latitudes. Although the (non-averaged) Sverdrup component away from the western boundary was upward due to the northward geostrophic flow as assumed by the Stommel-Arons model (e.g., Figure 13b), the southward western boundary current (mostly geostrophic) whose transport was larger than the northward interior geostrophic flow made the Sverdrup component downward there, which compensated the weak upward Sverdrup component in the interior.

The SA experiment illustrates importance of geostrophic flows not only for the horizontal structure of the Stommel-Arons thermohaline circulation but also for its vertical structure: the MOC. In the SA experiment, the east-west temperature difference, a key for the geostrophic MOC (Φ_g), was established primarily by the Kelvin waves which propagated cold temperature anomaly southward along the western boundary, leaving the southward (mostly geostrophic) western boundary current. (The Rossby waves on the other hand set the northward interior geostrophic flow.) Weaker the Kelvin wave propagation, the MOC more localized near the forcing region (e.g., Greatbatch and Lu 2003). In such cases, relative importance of the ageostrophic MOC (Φ_a) would increase.

5. Concluding Remarks and Discussions

This study evaluated the geostrophic and ageostrophic processes in the MOC using equations derived to diagnose vorticity balance and vertical velocity. To illustrate applicability of the equations, we at first revisited the MOC in an idealized rectangular ocean forced by zonally uniform differential surface heating and cooling. The diagnostic vorticity balance equation shows that the simulated MOC was primarily geostrophic, as described in the previous numerical studies (e.g., Bryan 1987; Zhang et al. 1992; Marotzke 1997; Spall and Pickart 2001; Scott and Marotzke 2002). The zonal tilt of the thermocline depth (or isopycnal surfaces) is thus a key for the MOC, and vertical mixing, known as a key ingredient in sustaining the MOC, affects the MOC by changing the zonal tilt (Zhang et al. 1992; Marotzke 1997; Scott and Marotzke 2002). Nonuniformly intensified vertical mixing can either strengthen or weaken the tilt, and hence the MOC. The point to emphasize in this study is that stronger vertical mixing does not always intensify the MOC, though it always tends to warm the deeper water. Note that the vertical advection - diffusion balance (Eq. 1) was still valid in the interior upwelling dominated region; this balance primarily determines $T(z)$ or thermocline depth with prescribed K_V and w (e.g., Bryan 1987; Zhang et al. 1992) rather than to control w with prescribed K_V and temperature profile $T(z)$. Intense upwelling/downwelling of the simulated MOC was found along lateral boundaries, as was shown by recent simulations (e.g., Spall and Pickart 2001; Katsman et al. 2018). The diagnostic equation for the vertical velocity shows that the geostrophic flows normal to the lateral boundaries induced the upwelling and downwelling along the boundaries and were the largest component in the simulation. Neither the Sverdrup interior (geostrophic) component nor the interior ageostrophic component was strong enough to sustain the simulated large-scale MOC. The MOC driven by localized cooling on the other hand showed that the interior ageostrophic component was large at around the forcing latitude while the the geostrophic flows normal to the lateral boundaries induced upwelling at other latitudes. This clearly illustrates that the ageostrophic processes feature the small-scale MOC, while the geostrophic processes shape the large-scale MOC.

In the real ocean, variable bottom and coastal topography as well as spatially-varying surface forcing may enlarge the ageostrophic MOC. For example, realistic simulation of the Pacific (Kawasaki et al. 2021) shows that the simulated MOC is similar to the geostrophic MOC for large scales, while the deviation from the geostrophic MOC is evident for small scales (Figure 16). Each MOC should be evaluated if such small-scale overturnings are to be discussed. Katsman et al. (2018) argued the along-boundary downwelling simulated in their realistic OGCM in terms of the along-coast density gradient (that induces geostrophic flow normal to the boundary), based on theoretical analysis by Spall and Pickart (2001). We believe that Eq. (24) will be useful to diagnose the intense upwelling/downwelling along the boundaries even in realistic OGCMs.

The MOC transports heat and alters temperature field, and the altered temperature field may change surface heat flux, stratification, and the vertical mixing. Thus, the entire processes between the MOC and the vertical mixing in the real ocean are nonlinear and complicated. If the MOC is found to be dominated by the geostrophy, then the question to be solved is the relation between the hydrostatic pressure (temperature) field and the mixing. Adjustments by the Rossby waves and the Kelvin waves will be one of key processes. Thus, diagnostic evaluation of the vorticity balance of the MOC using Eq. (17) and vertical velocity using Eq. (24) will be a first step to resolve such complicated processes. Such diagnostic evaluations may also be useful to reveal unexplored effects of the vertical mixing on the MOC. For example, vertical variation in the vertical mixing has been recently suggested to play an important role in abyssal overturning circulations (e.g., Ferrari 2014; McDougall and Ferrari 2017). The vertical eddy diffusivity is generally larger near the bottom due to larger turbulence, indicating more mixing with deeper (more dense) water than with shallower (less dense) water. This makes the deeper water more dense by turbulent mixing and hence the deeper water tends to sink, except for the water very close to the bottom boundary across which turbulent transport is negligible. Thus upwelling is expected to occur very close to the bottom boundary. It should be noted that this upwelling is expected to be diagnosed as the interior ageostrophic component. Thus, Eqs. (17) and (24) will be useful to quantitatively evaluate how and where this process dominates. This will be our future study.

Acknowledgments. Instructive comments from two anonymous reviewers help were helpful to improve this manuscript. This work was supported by JSPS KAKENHI Grant numbers JP15H05817/JP15H05824/JP15H05825.

References

Beardsley, R. C., and J. F. Festa, 1972: A numerical model of the convection driven by a surface stress and non-uniform horizontal heating. *Journal of Physical Oceanography*, **2**, 444 – 455.

Bryan, F., 1987: Parameter sensitivity of primitive equation ocean general circulation models. *Journal of Physical Oceanography*, **17 (7)**, 970 – 985.

Ferrari, R., 2014: What goes down must come up. *Nature*, **513 (7517)**, 179–180, doi:10.1038/513179a.

Greatbatch, R. J., and J. Lu, 2003: Reconciling the Stommel box model with the Stommel - Arons model: A possible role for southern hemisphere wind forcing? *Journal of Physical Oceanography*, **33**, 1618 – 1632, doi:10.1175/2411.1.

Hibiya, T., M. Nagasawa, and Y. Niwa, 2007: Latitudinal dependence of diapycnal diffusivity in the thermocline observed using a microstructure profiler. *Geophysical Research Letters*, **34 (24)**, doi:10.1029/2007GL032323.

Hirschi, J., and J. Marotzke, 2007: Reconstructing the meridional overturning circulation from boundary densities and the zonal wind stress. *Journal of Physical Oceanography*, **37 (3)**, 743 – 763, doi:10.1175/JPO3019.1.

Hughes, G. O., and R. W. Griffiths, 2008: Horizontal convection. *Annual Review of Fluid Mechanics*, **40**, 185 – 208, doi:10.1146/annurev.fluid.40.111406.102148.

Jayne, S. R., 2009: The impact of abyssal mixing parameterizations in an ocean general circulation model. *Journal of Physical Oceanography*, **7**, 1756 – 1774, doi:10.1175/2009JPO4085.1.

Katsman, C. A., S. S. Drijfhout, H. A. Dijkstra, and M. A. Spall, 2018: Sinking of dense north Atlantic waters in a global ocean model: Location and controls. *Journal of Geophysical Research*, **123**, 3563 – 3576, doi:10.1029/2017JC013329.

Kawasaki, T., and H. Hasumi, 2010: Role of localized mixing around the Kuril straits in the Pacific thermohaline circulation. *Journal of Geophysical Research*, **115 (C1102)**, doi:10.1029/2010JC006130.

Kawasaki, T., H. Hasumi, and Y. Tanaka, 2021: Role of tide-induced vertical mixing in the deep Pacific Ocean circulation. *Journal of Oceanography*, in press, doi:10.1007/s10872-020-00584-0.

Kawase, M., 1987: Establishment of deep ocean circulation driven by deep water formation. *Journal of Physical Oceanography*, **17**, 2294–2317.

Kuhlbrodt, T., 2008: On Sandström's inferences from his tank experiments: a hundred years later. *Tellus*, **60A (5)**, 819 – 836.

Ledwell, J. R., and A. J. W. C. S. Law, 1993: Evidence for slow mixing across the pycnocline from an open-ocean tracer-release experiment. *Nature*, **364**, 701 – 703, doi:10.1038/364701a0.

Ledwell, J. R., E. T. Montgomery, K. L. Polzin, L. C. S. Laurent, R. W. Schmitt, and J. M. Toole, 2000: Evidence for enhanced mixing over rough topography in the abyssal ocean. *Nature*, **403**, 179 – 182, doi:10.1038/35003164.

Ledwell, J. R., A. J. Watson, and C. S. Law, 1998: Mixing of a tracer in the pycnocline. *Journal of Geophysical Research*, **103**, 21 499 – 21 529, doi:10.1029/98JC01738.

Lee, T., and J. Marotzke, 1998: Seasonal cycles of meridional overturning and heat transport of the Indian ocean. *Journal of Physical Oceanography*, **28 (5)**, 923 – 943.

MacKinnon, J. A., and Coauthors, 2017: Climate process team on internal wavedriven ocean mixing. *Journal of Marine Research*, 2429 – 2454, doi:10.1175/BAMS-D-16-0030.1.

Marotzke, J., 1997: Boundary mixing and the dynamics of three-dimensional thermohaline circulation. *Journal of Physical Oceanography*, **27 (8)**, 1713–1728.

McDougall, T. J., and R. Ferrari, 2017: Abyssal upwelling and downwelling driven by near-boundary mixing. *Journal of Physical Oceanography*, **47**, 261 – 283, doi:10.1175/JPO-D-16-0082.1.

Munk, W., and C. Wunsch, 1998: Abyssal recipes ii: energetics of tidal and wind mixing. *Deep - Sea Research Part I*, **45**, 1977 – 2010, doi:10.1016/S0967-0637(98)00070-3.

Munk, W. H., 1966: Abyssal recipes. *Deep - Sea Research*, **13**, 707 – 730.

Park, Y.-G., and K. Bryan, 2000: Comparison of thermally driven circulations from a depth-coordinate model and an isopycnal-layer model. part i: Scaling-law sensitivity to vertical diffusivity. *Journal of Physical Oceanography*, **30**, 590–605.

Polzin, K. L., J. M. Toole, J. R. Ledwell, and R. W. Schmitt, 1997: Spatial variability of turbulent mixing in the abyssal ocean. *Science*, **276 (5309)**, 93 – 96, doi:10.1126/science.276.5309.93.

Rossby, T., 1998: Numerical experiments with a fluid heated non-uniformly from below. *Tellus*, **50A**, 242–257.

Scott, J. R., and J. Marotzke, 2002: The location of diapycnal mixing and the meridional overturning circulation. *Journal of Physical Oceanography*, **32 (12)**, 3578 – 3595.

Spall, M. A., 2000: Buoyancy-forced circulations around islands and ridges. *Journal of Marine Research*, **58 (3)**, 957 – 982.

Spall, M. A., and R. S. Pickart, 2001: Where does dense water sink? a subpolar gyre example. *Journal of Physical Oceanography*, **31 (3)**, 810 – 826.

Stommel, H., and A. B. Arons, 1960: On the abyssal circulation of the world ocean - i. stationary planetary flow patterns on a sphere. *Deep - Sea Research*, **6**, 140 – 154.

Tsujino, H., H. Hasumi, and N. Suginohara, 2000: Deep Pacific circulation controlled by vertical diffusivity at the lower thermocline depth. *Journal of Physical Oceanography*, **30 (11)**, 2853 – 2865, doi:10.1175/1520-0485(2001)031⟨2853:DPCCBV⟩2.0.CO;2.

Visbeck, M., 2007: Power of pull. *Nature*, **447**.

Waterhouse, A. F., and Coauthors, 2014: Global patterns of diapycnal mixing from measurements of the turbulent dissipation rate. *Journal of Physical Oceanography*, **44 (7)**, 1854 – 1872, doi:10.1175/JPO-D-13-0104.1.

Webb, D. J., and N. Suginohara, 2001: Vertical mixing in the ocean. *Nature*, **409 (37)**, doi:10.1038/35051171.

Wunsch, C., 2002: What is the thermohaline circulation. *Science*, **298 (5596)**, 1179 – 1181, doi:10.1126/science.1079329.

Zhang, S., C. A. Lin, and R. J. Greatbatch, 1992: A thermocline model for ocean-climate studies. *Journal of Marine Research*, **50**, 99 – 124.

LIST OF FIGURES

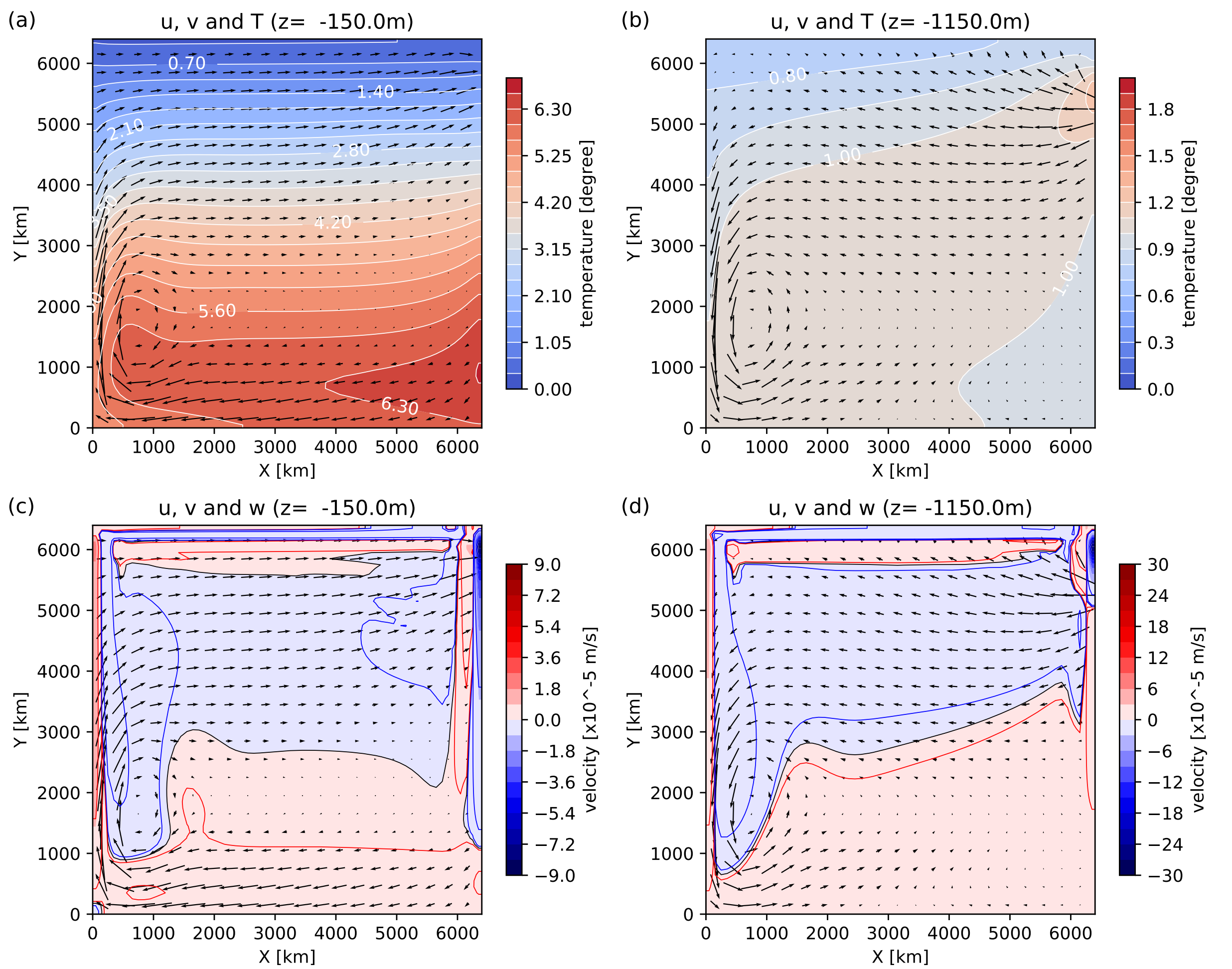

FIG. 1. (a, b) Temperature and (c, d) vertical velocity with horizontal velocity vectors at (a,c) $z = -150$ m and (b,d) $z = -1150$ m in the B experiment. In (c) and (d), colors are shaded in linear scale but contour lines are drawn in logarithmic scale ($10^{-7}, 10^{-6.5}, 10^{-6}, 10^{-5.5}, 10^{-5}, 10^{-4.5}$ m s^{-1} in magnitude).

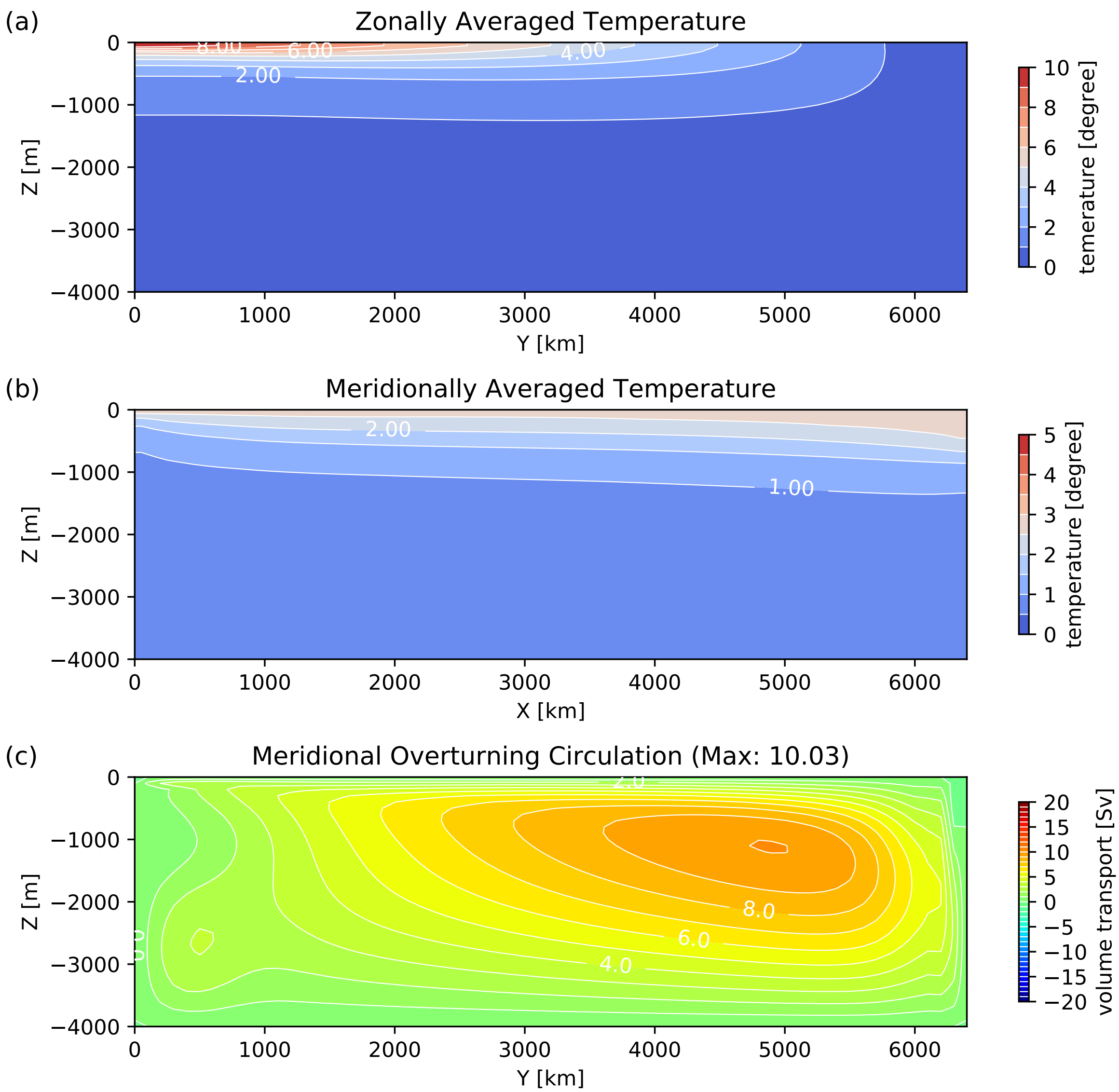

FIG. 2. (a) Meridional section of zonally averaged temperature. (b) Zonal section of temperature averaged over 4600 km $\leq y \leq$ 5000 km. (c) Meridional volume transport function (Φ). Results from the B experiment are shown.

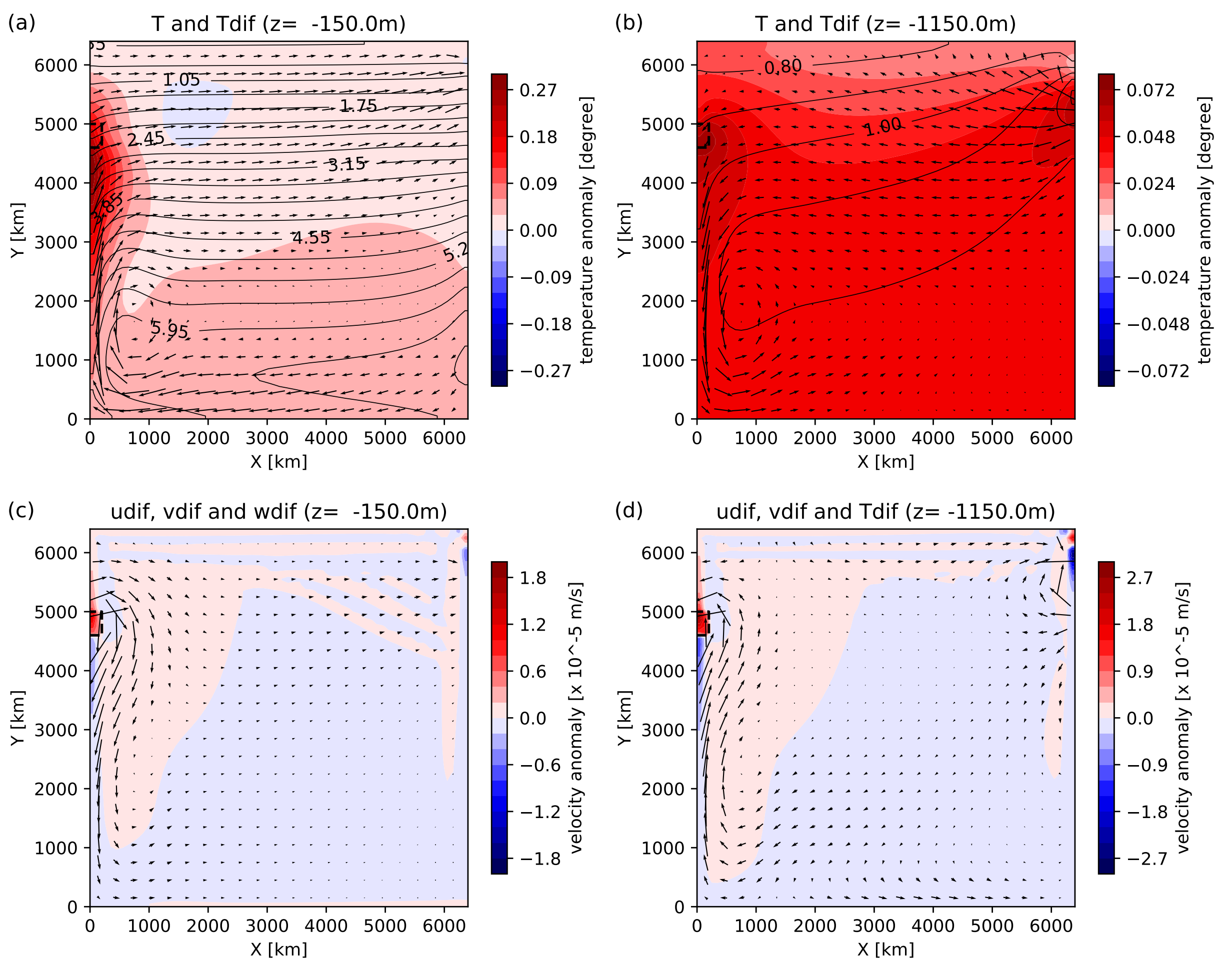

FIG. 3. (a, b) Temperature (contour) and horizontal velocity (arrows) in the W experiment at (a) $z = -150$ m and (b) $z = -1150$ m. Color represents temperature anomaly from the B experiment (W experiment - B experiment). (c, d) Anomaly of horizontal velocity (arrows) and vertical velocity (color) in the W experiment from the B experiment at (c) $z = -150$ m and (d) $z = -1150$ m.

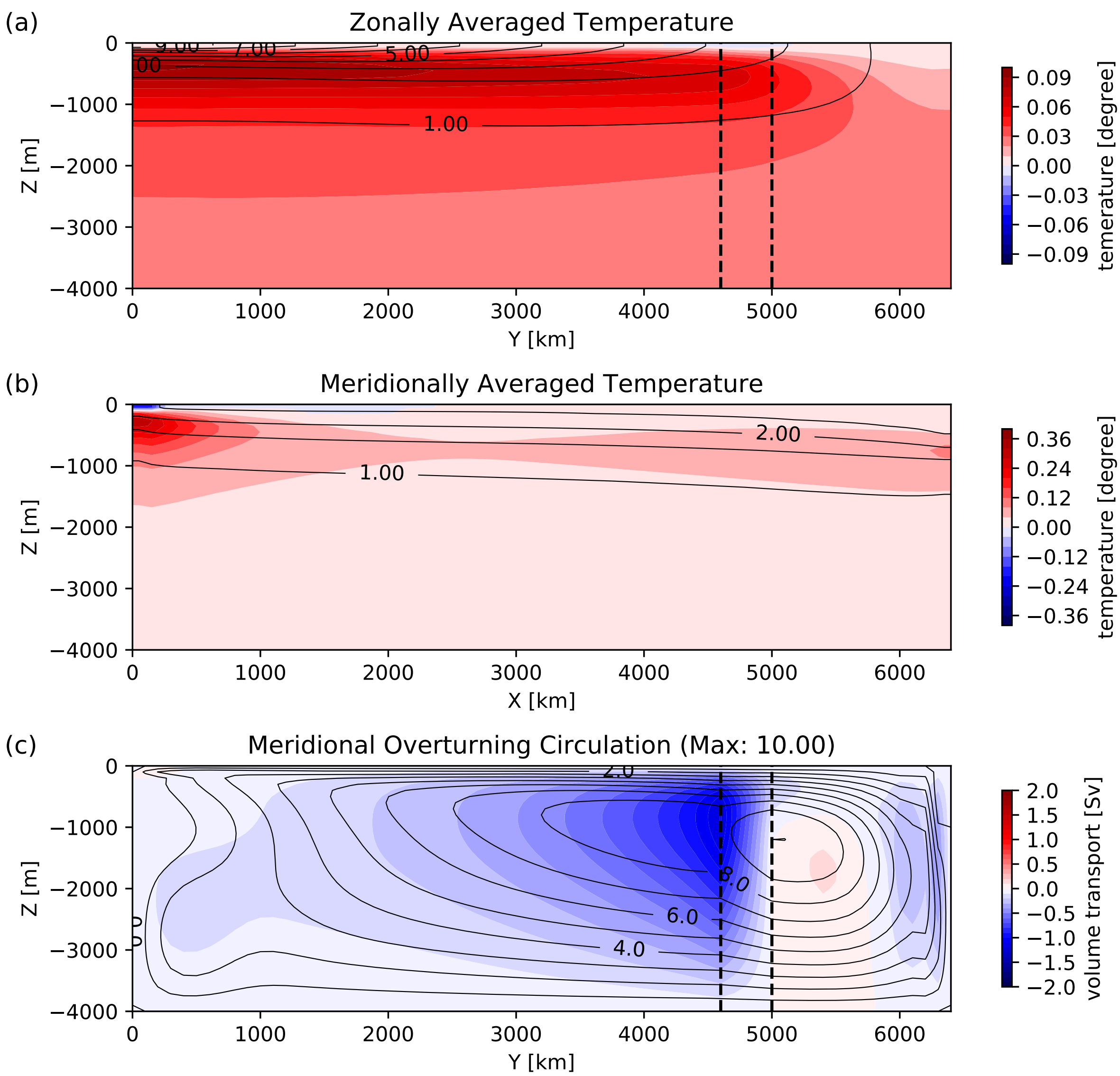

FIG. 4. Same as Figure 2 but for the W experiment. Color represents anomaly from the B experiment. Vertical dashed lines denote the intensified mixing region.

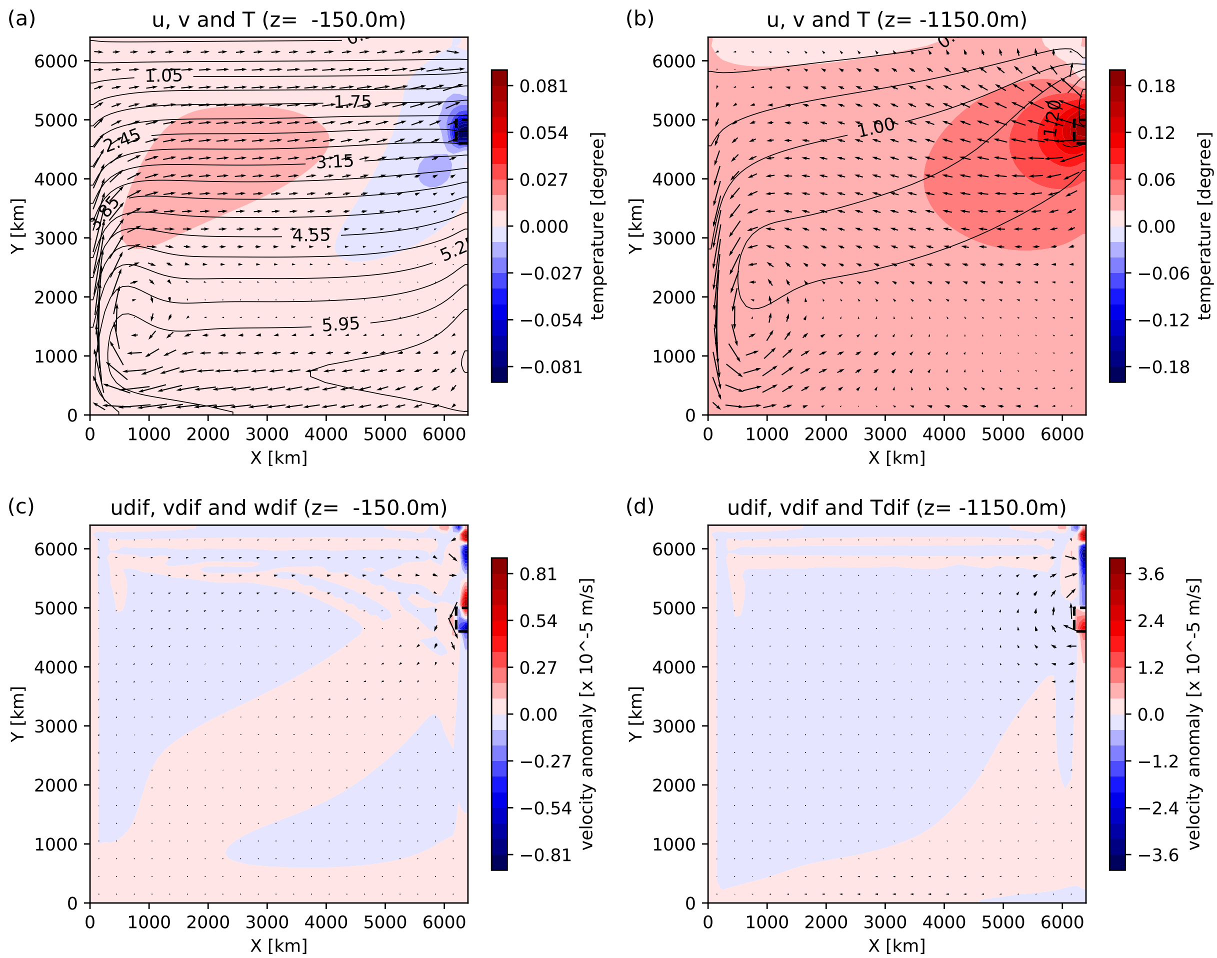

FIG. 5. Same as Figure 3 but for the E experiment.

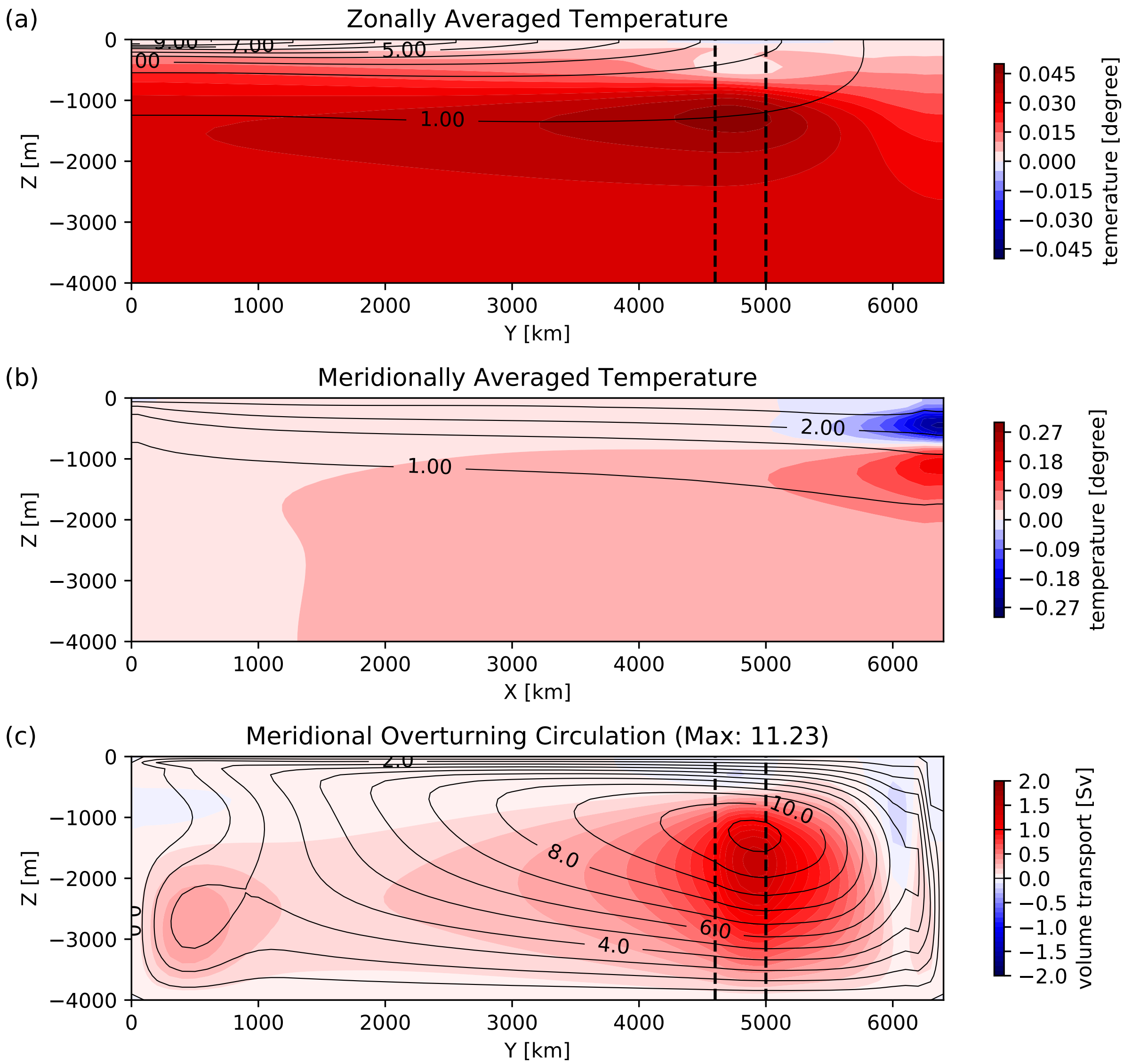

FIG. 6. Same as Figure 4 but for the E experiment.

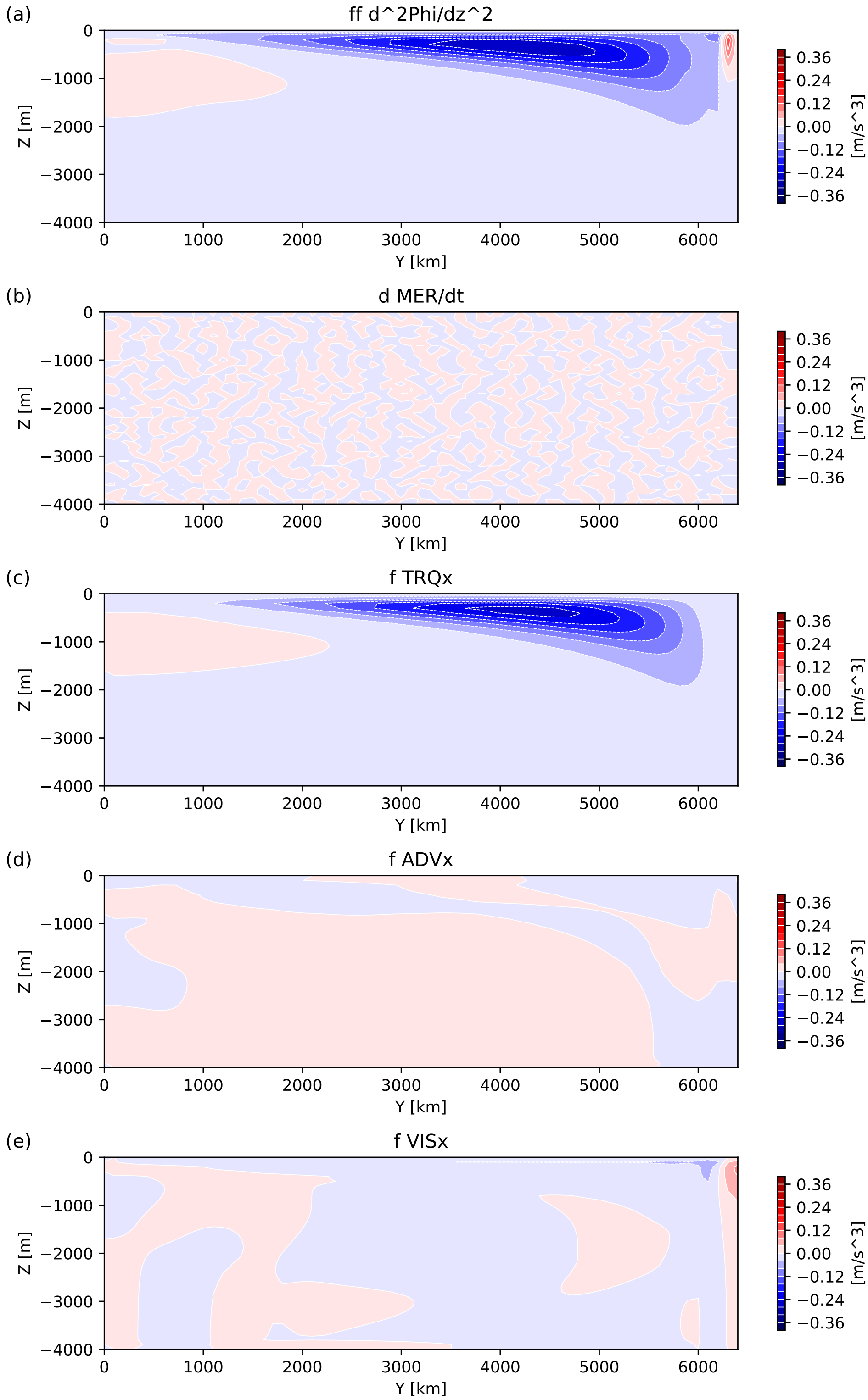

FIG. 7. Terms in Eq. (17): (a) the left-hand side term ($f^2\partial\Phi/\partial z^2$, second time derivative ignored), (b) the first line in the right hand side, (c) the first term ($-f\alpha g(T_E - T_W)$), (d) the second term ($-f\int_0^L \partial\mathscr{A}(u)/\partial z dx$), and (e) the last term ($f\int_0^L \partial\mathscr{V}(u)/\partial z dx$) in the second line in the right hand side .

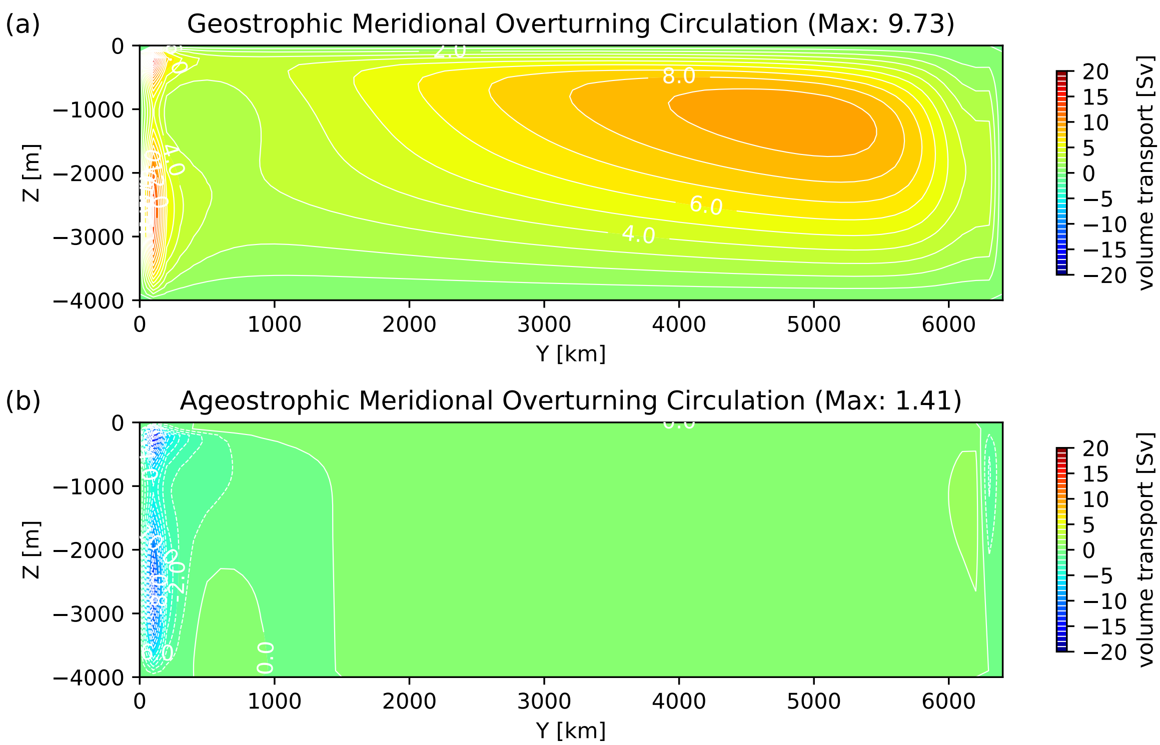

FIG. 8. Same as Figure 2c but for (a) geostrophic component (Φ_g) and (b) ageostrophic component (Φ_a).

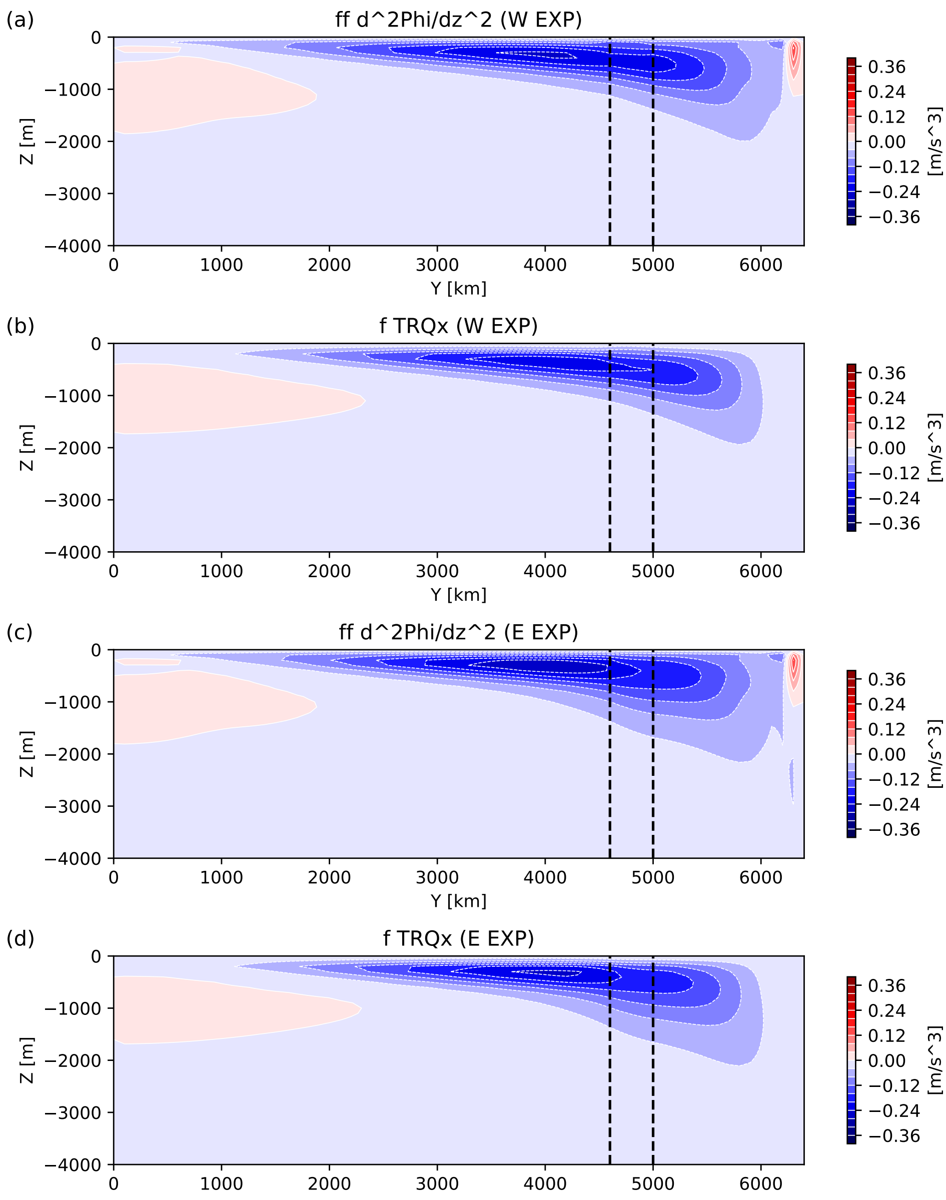

FIG. 9. Same as (a,c) Figure 7a and (b,d) Figure 7c but for (a,b) the W experiment and (c,d) the E experiment.

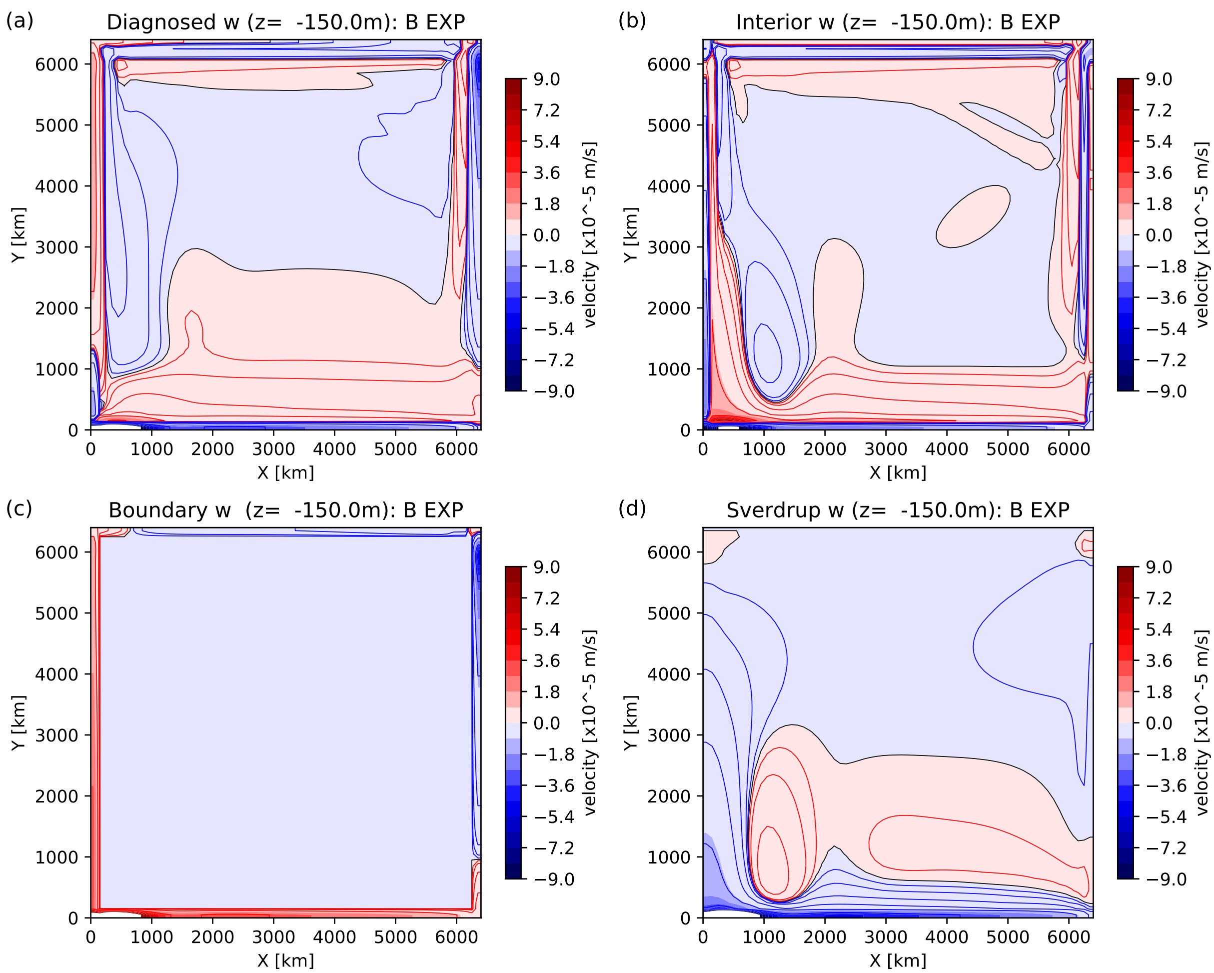

643 FIG. 10. Diagnosed vertical velocities from Eq. (24): (a) total (the left hand side), (b) interior ageostrophic
644 component (the first term of the right hand side evaluated at interior grid points), boundary ageostrophic com-
645 ponent (the first term of the right hand side) evaluated at boundary grid points, and (d) Sverdrup component (the
646 second term of the right hand side). Color and contour intervals are same as those in Figure 1c.

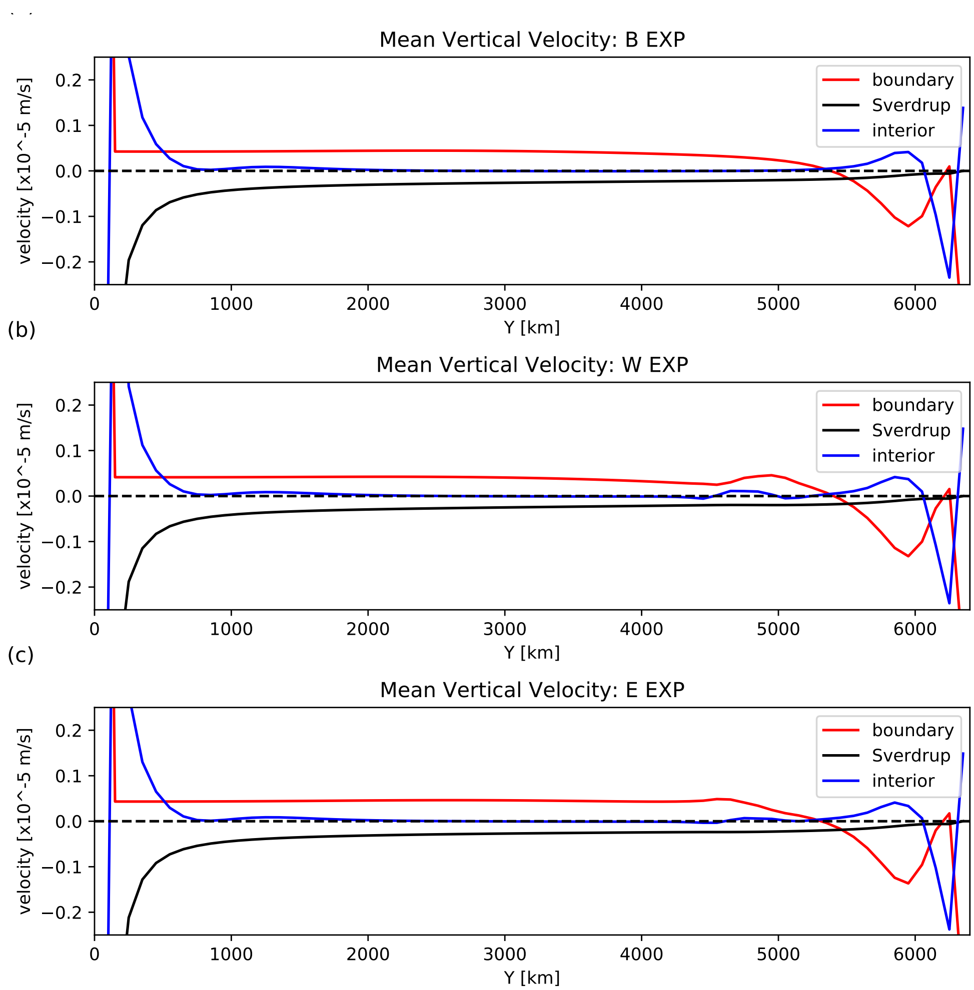

FIG. 11. Meridional profiles of the mean vertical velocity components (interior ageostrophic, boundary ageostrophic and Sverdrup components) averaged over zonal - vertical (x - z) section. (a) B experiment, (b) W experiment, and (c) E experiment. Large values at the southern end ($y = 0$) were errors due to small f.

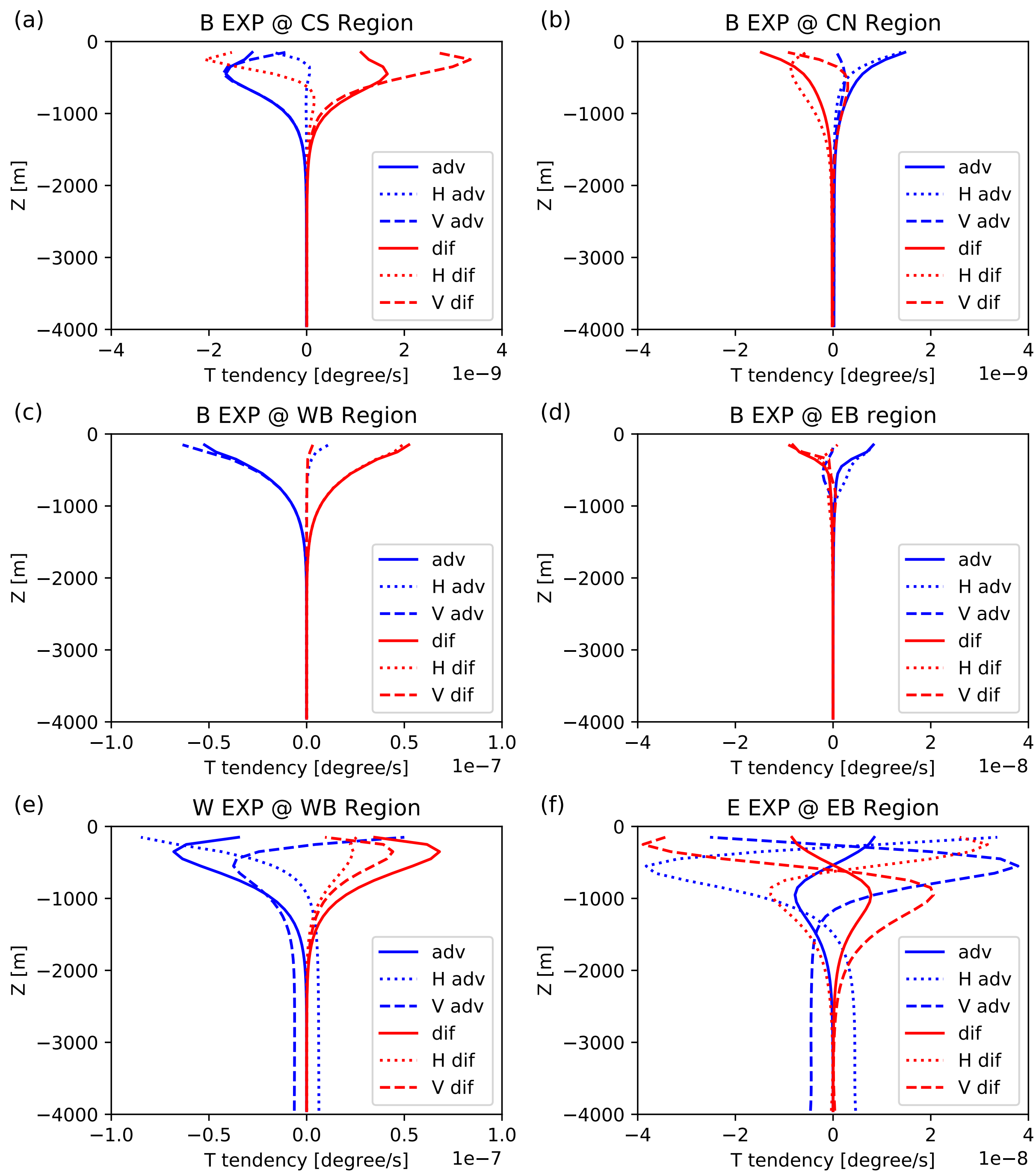

FIG. 12. Vertical profiles of temperature tendency terms. (a) Central southern region (3000 km $\leq x \leq$ 3400 km and 1400 km $\leq y \leq$ 1800 km), (b) central northern region (3000 km $\leq x \leq$ 3400 km and 6200 km $\leq y \leq$ 6600 km), (c) in the western boundary region ($x \leq$ 200 km and 6200 km $\leq y \leq$ 6600 km, the intensified mixing region in the W experiment) and (d) in the eastern boundary region (6200 km $\leq x$ and 6200 km $\leq y \leq$ 6600 km, the intensified mixing region in the E experiment) of the B experiment. (e) Same as (c) but for the W experiment. (f) Same as (d) but for the E experiment. Blue and red lines represent advection and diffusion terms, respectively. Dotted and dashed lines are horizontal and vertical components, respectively, while solid lines are sum of the components.

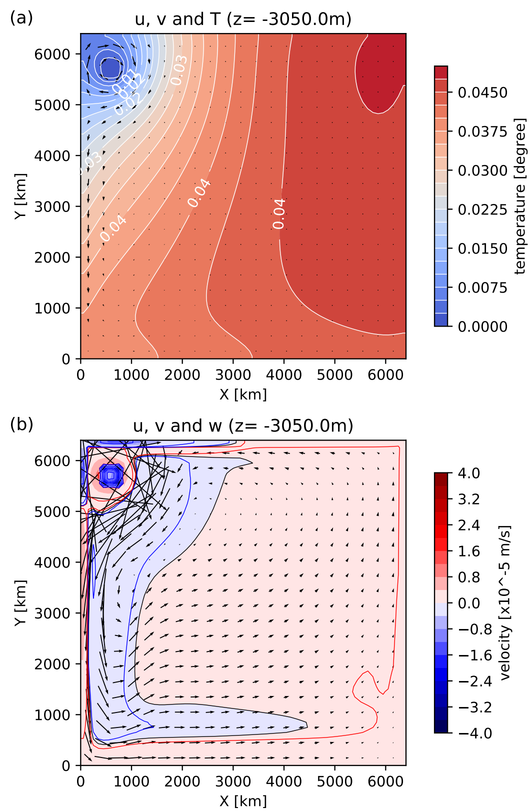

FIG. 13. Horizontal distributions at $z = -3050$ m of (a) temperature and (b) vertical velocity with horizontal velocity vector in the SA experiment. Arrows in (b) is magnified by 10 times for better identifying weak interior flows.

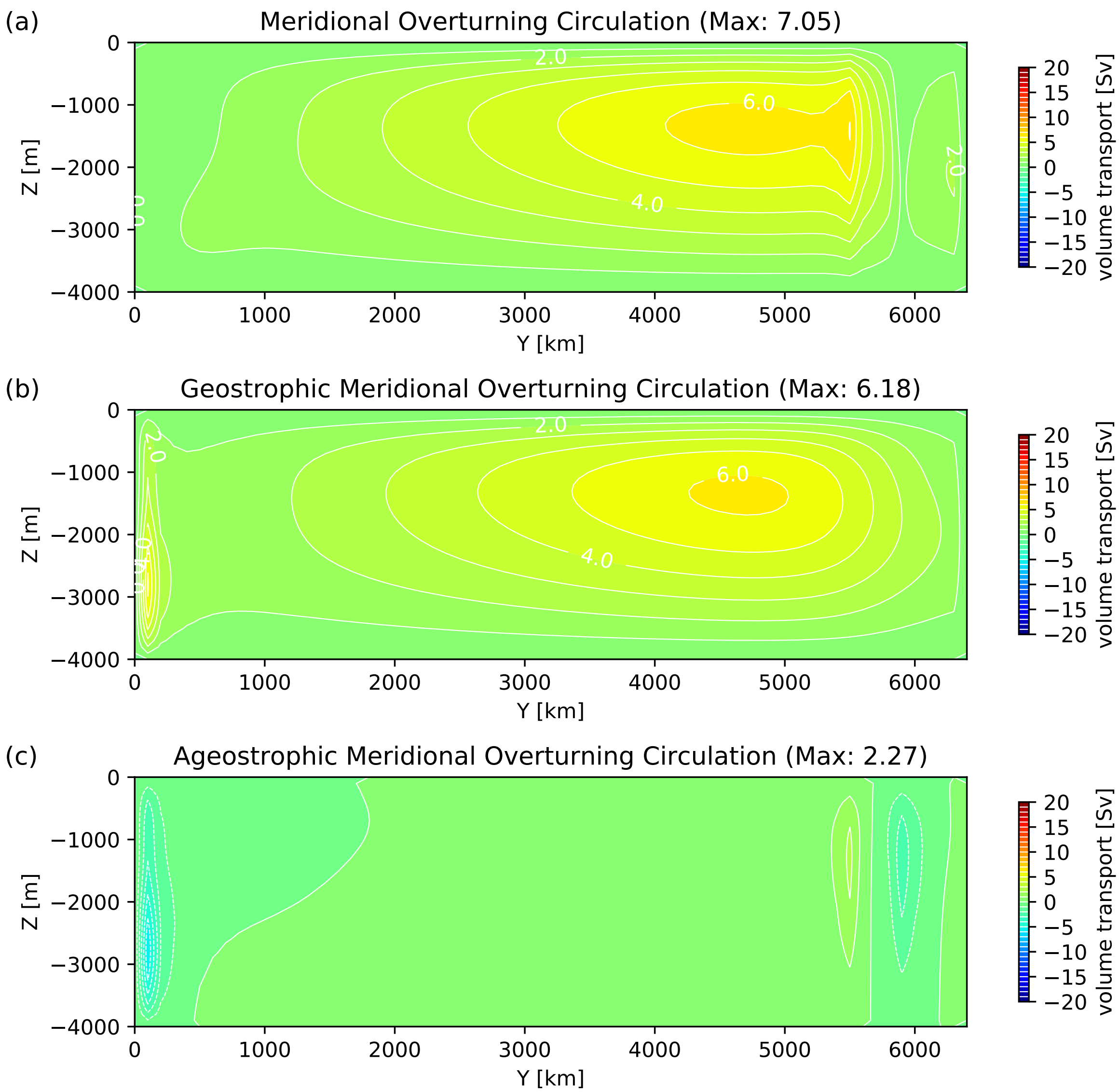

FIG. 14. Meridional volume transport functions in the SA experiment. (a) Total (Φ). (b) Geostrophic component (Φ_g). (c) Ageostrophic component (Φ_a).

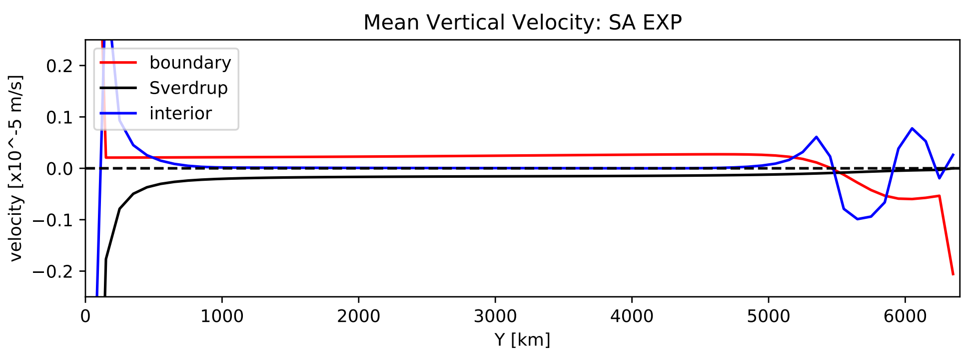

FIG. 15. Same as Figure 11 but for the SA experiment.

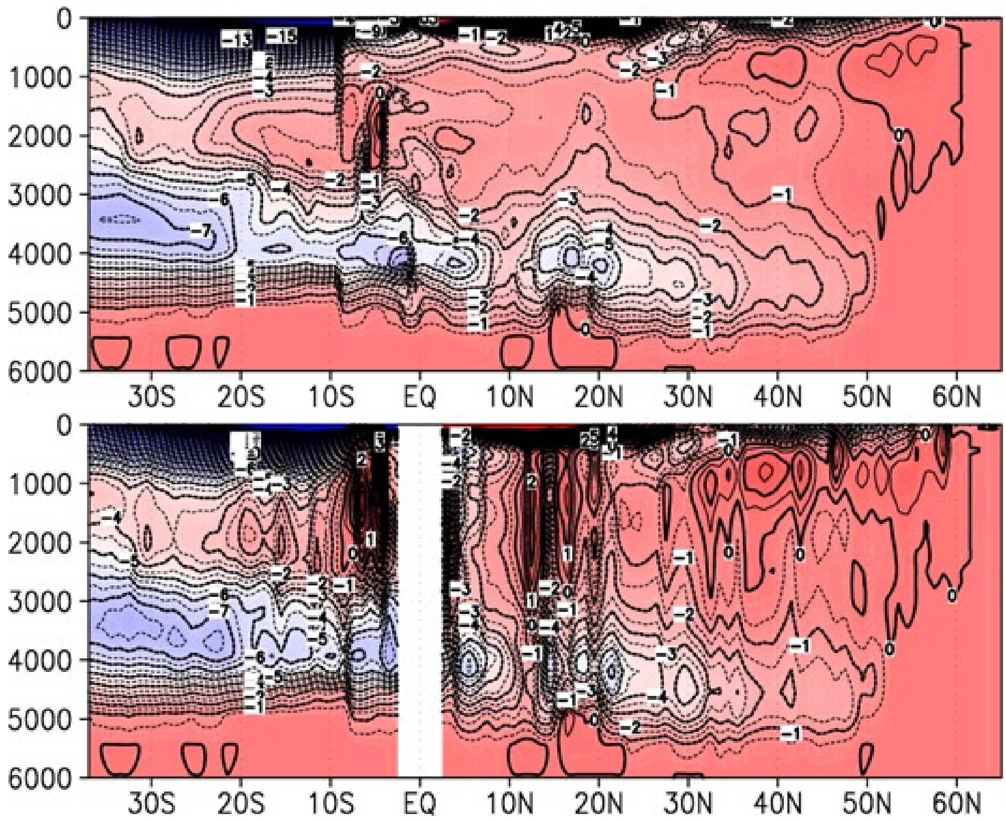

FIG. 16. MOCs in the Pacific simulated in the realistic OGCM of Kawasaki et al. (2021). (a) Total component (Φ). (b) Geostrophic component (Φ_g).